J. Fluid Mech. (1998), *vol.* 377, *pp.* 223–252. Printed in the United Kingdom

Internal wave excitation from stratified flow over a thin barrier

By BRUCE R. SUTHERLAND† AND PAUL F. LINDEN

Department of Applied Mathematics and Theoretical Physics, University of Cambridge, Silver Street, Cambridge, CB3 9EW, UK

(Received 11 November 1997 and in revised form 27 July 1998)

We perform laboratory experiments in a recirculating shear flow tank of non-uniform salt-stratified water to examine the excitation of internal gravity waves (IGW) in the wake of a tall, thin vertical barrier. The purpose of this study is to characterize and quantify the coupling between coherent structures shed in the wake and internal waves that radiate from the mixing region into the deep, stationary fluid. In agreement with numerical simulations, large-amplitude internal waves are generated when the mixing region is weakly stratified and the deep fluid is sufficiently strongly stratified. If the mixing region is unstratified, weak but continuous internal wave excitation occurs. In all cases, the tilt of the phase lines of propagating waves lies within a narrow range. Assuming the waves are spanwise uniform, their amplitude in space and time is measured non-intrusively using a recently developed 'synthetic schlieren' technique. Using wavelet transforms to measure consistently the width and duration of the observed wavepackets, the Reynolds stress is measured and, in particular, we estimate that when large-amplitude internal wave excitation occurs, approximately 7% of the average momentum across the shear depth and over the extent of the wavepacket is lost due to transport away from the mixing region by the waves.

We propose that internal waves may act back upon the mean flow modifying it so that the excitation of waves of that frequency is enhanced. A narrow frequency spectrum of large-amplitude waves is observed because the feedback is largest for waves with phase tilt in a range near 45°. Numerical simulations and analytic theories are presented to further quantify this theory.

1. Introduction

Internal gravity waves (IGW) are generated whenever the fluid is perturbed at frequencies less than its natural buoyancy frequency. Such excitation occurs naturally in many geophysical circumstances. Probably the best known example of this phenomenon is the generation of mountain waves, a manifestation of IGW that occur when sufficiently strongly stratified air is vertically displaced as it flows over orography. The transport of momentum by these waves is now well known to contribute significantly to the general circulation of the atmosphere (for example, see Bretherton 1969; Lilly & Kennedy 1973; McFarlane 1987; Palmer, Shutts & Swinbank 1986). Likewise, IGW may be generated due to the flow of stratified water over sea mounts and sills; a classic example is the excitation of internal solitary waves in the Strait of Gibraltar (for example, see Lacombe & Richez 1982; Brandt, Alpers & Backhaus

† Present address: Department of Mathematical Sciences, University of Alberta, Edmonton, Alberta, Canada.

1996), Recently, mechanisms other than orographic excitation have been examined including convective forcing (for example, see Fovell, Durran & Holton 1992; Alexander 1996) and shear instability (for example see Davis & Peltier 1979; Fritts 1982; Chimonas & Grant 1984; Sutherland, Caulfield & Peltier 1994).

A dramatic visualization of IGW in the atmosphere can occur under partly cloudly conditions when moisture condenses at the crests of the waves thus rendering them visible as banded cloud patterns†. The preponderance of almost periodic wave trains made visible by clouds is a curiosity, however. Often IGW exhibit such periodicity even though local topographic features are irregular, and over flat land and sea periodic cloud patterns are nonetheless observed. The processes leading to the generation of periodic IGW under these circumstances remain poorly understood.

Laboratory experiments on stratified turbulence suggest that nonlinear mechanisms may contribute significantly to the mechanism whereby quasi-periodic IGW are generated. For example, in mixing box experiments performed by Linden (1975) a fully turbulent region near the surface of an initially linearly stratified fluid was established by a vertically oscillating horizontal grid. As the experiment progressed transient IGW excitation was observed below the base of the mixing region and, although the turbulence exhibited motion with a broad range of frequencies, the waves themselves occurred within a relatively narrow frequency band. Specifically, IGW were observed to propagate below the mixing region with phase lines tilting at angles ranging from 0° to 35° with the vertical. Estimates of the wave amplitudes suggested that significant energy radiated from the turbulent region. Similar results were observed in experiments performed in linearly stratified fluid of the wake behind a horizontal cylinder (for example Stevenson & Thomas 1969; Lin & Pao 1979; Boyer *et al.* 1989) and behind a sphere (for example Lin, Boyer & Fernando 1992; Bonneton, Chomaz & Hopfinger 1993). In each case, observed waves propagated away from the turbulent region in a limited band of frequencies close to the buoyancy frequency.

These observations lead us to propose that periodic IGW occur when they are capable of acting back upon the mixing region in a way that further enhances their excitation, an assertion that we attempt to demonstrate both qualitatively and quantitatively here.

As with any feedback process, the influence of IGW back upon the mixing region is a nonlinear mechanism that acts significantly when motions near the base of the mixing region are of sufficiently large amplitude. Numerical simulations have shown that this feedback is a robust feature of dynamically unstable flows in non-uniform stratification (Sutherland *et al.* 1994). The specific criterion for strong emission ('strong' in the sense that the mean flow experiences non-negligible drag due to the transport of momentum away from the mixing region by IGW) is defined in terms of two buoyancy parameters, J_{mix} and J_{deep}. Under the Boussinesq approximation the squared buoyancy frequency N^2 is defined in terms of the ambient density gradient $\overline{\rho}(z)$ by $N^2 = -(g/\rho_{00})\mathrm{d}\overline{\rho}(z)/\mathrm{d}z$, in which ρ_{00} is the characteristic density. Then in the mixing region (where there is strong shear and overturning and entrainment occurs) $J_{\mathrm{mix}} = N_{\mathrm{mix}}^2 L^2/U^2$, in which N_{mix} is the buoyancy frequency evaluated at a vertical level where the shear is largest, and U and L are the characteristic velocity and length scales, respectively, of the shear flow. In the far field (where there is no background shear and no mixing, only wave propagation) $J_{\mathrm{deep}} = N_{\mathrm{deep}}^2 L^2/U^2$, in which N_{deep}

† At the time of writing, excellent photographs taken by satellite and by space shuttle astronauts of internal gravity waves in the atmosphere and ocean appear on the NASA World Wide Web site: *http://www.nasa.gov/gallery/photo/*.

is the characteristic buoyancy frequency below the mixing region. By examining the growth and nonlinear development of the most unstable normal mode of an unstable hyperbolic tangent shear flow with non-uniform stratification in a periodic channel, Sutherland (1996) has shown that strong excitation occurs if $J_{\rm mix} \lesssim 1/4$ and $J_{\rm deep} \gtrsim 1/4$. This mechanism for IGW excitation has been proposed as a source of non-hydrostatic upward propagating IGW due to shear instability of the upper flank of the tropospheric jet (Sutherland & Peltier 1995) and of downward propagating IGW generated by shear instability of the upper flank of the equatorial undercurrent (Sutherland 1996).

As part of this work, we perform laboratory experiments to examine the shear excitation of IGW in the wake of salt-stratified flow over a thin barrier. Unlike many studies of sheared stratified turbulence, we study the behaviour of non-uniformly stratified fluid. Typically, the region where mixing occurs is more weakly stratified initially than the deep stationary fluid where IGW propagation occurs. The experiment has been set up in this way because numerical simulations predict that large-amplitude IGW may be generated under such circumstances and, hence, the interactions between the mixing region and radiating IGW may be more easily observed. The dynamics of the experimental flow differ from the numerical studies in which the flow is horizontally periodic and the disturbances grow in time. Here the shear instability is a spatially growing disturbance.

Analytic solutions of uniformly stratified constant upstream flow over a thin barrier have been found previously by Miles (1968) (see also figure 3 of Huppert & Miles 1969), although his calculations showed that the flow is unstable (in the sense of Long (1955) that the solution has closed streamlines) to wavelengths small compared with $4.0U_c/N_c$, in which U_c is the upstream flow speed and N_c is the buoyancy frequency. Although laboratory experiments have been performed to study the flow over a thin barrier with the upstream conditions prescribed by Miles (1968) (Davis 1969; Castro, Snyder & Baines 1990), ours differ from these conditions in two significant ways: the barrier is large compared with the fluid depth, extending over approximately 80% of the fluid depth; the upstream flow and stratification is non-uniform, the flow being non-zero only over the top 20% of the fluid depth and the stratification in the mixing region being generally smaller than the stratification of the deeper fluid. Accordingly, our focus is not on the generation and upward propagation of IGW that occur on the scale of the lee waves. Rather we examine the generation and downward propagation of IGW that occur on the scale of coherent structures that develop from shear instabilities immediately in the wake of the barrier. In the light of the prediction of Miles (1968), it is reasonable to expect that instabilities should occur due to wavelengths on the order of $U/N_{\rm mix}$. Indeed, in experiments with a moderately stratified mixing region vortex shedding occurs on length scales in this range.

IGW characteristics are determined by a variety of methods including conductivity probe measurements at a fixed depth which give the fluctuation density in time at a point, and dye line tracking which gives the fluctuation horizontal velocity along a vertical line. We make extensive use of a 'synthetic schlieren' technique (Dalziel, Hughes & Sutherland 1998) by which the instantaneous two-dimensional wave field can be quantitatively but non-intrusively determined. These methods will be described in some detail in §2.

In §3 we describe qualitatively the experimental results. In particular, we demonstrate the excitation of IGW in three experiments, each with similar deep stratification but with weak, moderate, and strong stratification in the mixing region. Time series demonstrate the coupling between coherent structures in the lee and radiating IGW.

Adapting the technique developed by Alexander (1996), we employ a wavelet analysis in §4 to provide consistent estimates of the extent and amplitude of the observed wavepackets, and to compute the momentum flux across a fixed vertical level. The analyses show that the drag exerted on the mixing region due to the extraction of momentum by IGW is significant when strong IGW emission occurs: the mean flow over the horizontal extent of the wavepacket can be decelerated by approximately 7% of the characteristic flow speed over the shear half-depth.

To illustrate and quantify further the effect of IGW excitation back upon the mixing region, we have performed a series of numerical simulations, which are reported in §5. The initial basic state, a hyperbolic tangent shear flow in non-uniform stratification, is similar to that examined by Sutherland (1996). However, instead of simulating the nonlinear development of a horizontally periodic normal mode, here we study the horizontal spatial as well as temporal evolution of a localized perturbation to the vorticity field in the shear flow. We show that the mixing region itself undergoes a significantly modified evolution when the deep fluid is sufficiently strongly stratified to allow the generation of IGW.

Some simple arguments based on linear theory are proposed in §6 to explain why IGW are frequently observed in a limited range of frequencies.

2. Experimental setup

Experiments are performed in a recirculating tank as shown schematically in figure 1. The test section of the tank is 40 cm deep, 20 cm wide and over 2 m long. Using a 'double bucket' system, the tank is filled with salt-stratified water to a depth of approximately 35 cm. The stratification near the surface is reduced between successive experiments by mixing which occurs over the top 10 cm. Over time, a surface mixing region develops due to convection driven by evaporation. During the many days over which a series of experiments is typically performed, this unstratified region can extend down to approximately 3 cm below the surface, and in some experiments the region can significantly affect the large-scale structure of the downstream flow. Its direct influence upon the generation of IGW is likely to be a secondary effect because, as we will show, the length scale relevant to the dynamics of IGW generation is of order 1 cm, much less than the depth (approximately 5 cm) of the mixing region downstream of the barrier.

A Kovasznay-type motor (Odell & Kovasznay 1971) generates a shear flow near the surface. The motor is composed of two stacks of horizontally oriented disks that rotate about their vertical axes, and which accelerate the interstitial fluid within their viscous boundary layers. The three disks in each stack are situated between $z = 27$ and 35 cm above the bottom of the tank. Though the vertical structure of the resulting shear flow depends in part upon the structure of the vertical density profile, typically the fluid in the test section is stationary between $z = 0$ and 25 cm.

A 27 cm tall, 4 mm thick vertical barrier stands on the bottom of the tank and spans its width. The height of the barrier is chosen so that the vertical displacement of fluid passing over the barrier is small (on the order of 1 cm) compared with the barrier height. The shear flow upstream of the barrier is stable, as indicated by the propagation of vertical dye lines dropped up to 50 cm upstream. As the shear flow passes over the barrier lee waves and overturning regions occur downstream. The qualitative behaviour of the flow varies depending on the flow speed and local stratification. For the range of experiments performed, the upstream flow speed measured at the same depth as the top of the barrier ranges from about 0.5 cm s^{-1}

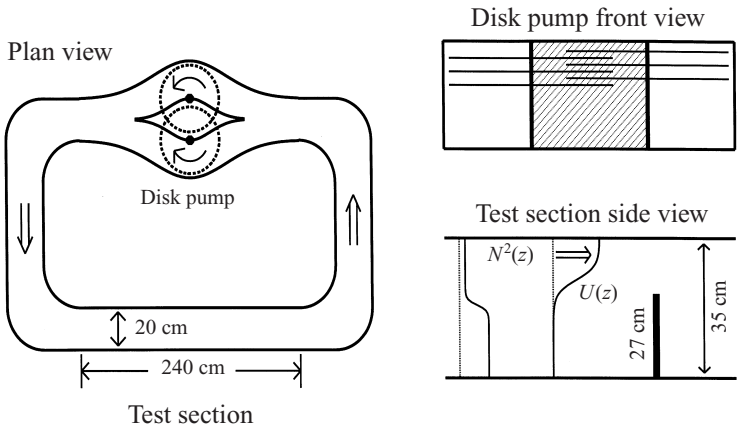

FIGURE 1. Schematic of the Kovasznay-type tank, in which a stratified shear flow near the surface of a recirculating tank is driven by two sets of interleaving rotating disks. Internal waves are generated in the lee of a 27 cm tall, thin vertical barrier that spans the width of the tank.

to 2.0 cm s^{-1}. The density structure near the same depth is either unstratified or stratified with buoyancy frequency as large as $N_{\mathrm{mix}} \simeq 1\ s^{-1}$. Typically, the deep water stratification is characterized by buoyancy frequency $N_{\mathrm{deep}} \simeq 1\ s^{-1}$. When large-amplitude internal waves occur the density gradient is observed to change locally due to stretching and compression of the isopycnals. This effectively changes the local value of the squared buoyancy frequency by up to 15% (i.e. $\Delta N^2/N^2 \lesssim 0.15$, in which $\Delta N^2 = -(g/\rho_{00})\partial\rho'/\partial z$, and ρ' is the perturbation density field).

The initial density profile $\overline{\rho}$ is measured with a conductivity probe that between brief acceleration and deceleration times is traversed vertically at 4 cm s^{-1} with a sampling rate of 100 Hz. In some experiments, successive traverses of the probe are periodically taken through the mixing region to measure the deepening of the mixed layer.

The flow in the mixing region itself is visualized by dye in two ways. The mean flow profile is determined by tracking the propagation of vertical lines of dye. To make the lines, 1 mm diameter glass beads coated with a concentrated solution of rhodamine dye are dropped into the flow at regular intervals. Shed vortices and the flow that passes near the top of the barrier are visualized by potassium permanganate crystals that are placed on top of the barrier and which slowly dissolve during the course of an experiment.

The wavelength, frequency, and amplitude of IGW are measured by a variety of techniques. By recording conductivity variations at a fixed level z_0 over time, vertical displacements below the base of the mixing region Δz may be estimated from the density fluctuations ρ' assuming the linear relationship

$$\Delta\rho'(t; z_0) = \Delta z(t; z_0)\mathrm{d}\overline{\rho}/\mathrm{d}z. \tag{2.1}$$

In addition, the horizontal motion of vertical lines of rhodamine dye in the deep fluid can be tracked from digitized images of the experiment to give the profiles of the fluctuation horizontal velocity along the line.

We make extensive use of a 'synthetic schlieren' technique by which we quantitatively, but non-intrusively measure the two-dimensional field of the IGW as it evolves in time (Sutherland *et al.* 1998). The technique consists of placing a back-illuminated grid of horizontal black lines behind the test section and recording the position of the lines using a CCD camera connected to an image processing system, *DigImage*. The

stretching and compression of isopycnals due to the passage of IGW locally changes the gradient of the index of refraction of the fluid so that the grid lines behind them appear to be displaced. At any time the vertical displacements of the grid lines, $\Delta z_G(x,z,t)$, from the initial grid line positions are used to calculate directly the change of the squared buoyancy frequency $\Delta N^2(x,z,t) = -(g/\rho_0)\mathrm{d}\rho'/\mathrm{d}z$. Explicitly,

$$\Delta N^2(x,z,t) = -\left[\gamma\left(\tfrac{1}{2}{L_T}^2 + n_w/n_a L_G L_T\right)\right]^{-1}\Delta z_G, \tag{2.2}$$

in which n_w and n_a are the indices of refraction of water and air, respectively, L_T is the span of the tank, and L_G is the distance from the tank to the grid of lines. The effect of the thickness of the tank walls, which is a negligible correction, has been omitted from the equation. The constant $\gamma = (1/g)(\rho_{00}/n_w)\mathrm{d}n/\mathrm{d}\rho \simeq 1.878 \times 10^{-4}$ s^2 cm^{-1}, in which g is the acceleration due to gravity, ρ_{00} is the density of water at room temperature, and $\mathrm{d}n/\mathrm{d}\rho$ is the rate of change of the index of refraction of salt water with density, which is approximately constant for the small salt concentrations used here.

In practice, Δz_G is determined by quadratic interpolation of the pixel intensity at one time with the initial intensity of the upper, middle and lower pixels. The intensity of a single pixel is the average digitized intensity of light over the pixel area, typically 0.2 mm^2. Interpolation is performed only when the intensity difference between the upper and lower pixels and the middle pixel exceeds some threshold. The pixels have digitized intensities ranging from 0 to 255 and, typically, a threshold is set at 25. The pixels excluded from the calculation are assigned to be the Gaussian weighted average of the surrounding included pixels. In this way, points within a standard deviation of 2 pixels contribute most significantly.

As well as calculating ΔN^2 as a function of the displacement of grid lines from their initial position, the time derivative of the squared buoyancy frequency, N_t^2, is found by calculating the displacement of grid lines between two short successive times (typically 0.4 s).

Ambient heat fluctuations in the laboratory can give rise to spurious noise. Because these fluctuations occur on a much faster time scale (1/10 s) than that of IGW (10 s), it is possible to filter them from the digitized signal by applying a low pass Fourier filter to time series constructed from the ΔN^2 and N_t^2 fields.

Figure 2 shows the ΔN^2 and N_t^2 fields between 5 cm upstream and 30 cm downstream of the barrier (at $x = 0$), and between 5 cm above and 20 cm below the top of the barrier (at $z = 0$). The ΔN^2 field is shown on a grey scale with black corresponding to $\Delta N^2 = -0.16$ s^{-2} and white corresponding to $\Delta N^2 = +0.16$ s^{-2}. Similarly, the N_t^2 field is shown on a grey scale corresponding to values ranging from -0.04 to 0.04 s^{-3}. The fields are calculated at a time when strong IGW radiate from the mixing region, the waves extending downward from left to right. Although the calculation is not valid in turbulent regions where the flow is not spanwise uniform, it is nonetheless useful to show these regions as they qualitatively indicate the flow structure in the mixing region. The panels show that a lee wave develops in the wake of the barrier, breaking after a half-period, approximately 10 cm downstream (see also figure 3). The IGW with phase tilts approximately 45° to the vertical are generated with horizontal wavelengths approximately 7 cm, smaller than the wavelength of the lee waves. As expected, the ΔN^2 field is out of phase with the N_t^2 field where propagating IGW occur. The ΔN^2 field also shows significant structure upstream of the barrier, which corresponds to the vertical compression (where $\Delta N^2 \simeq 0.16$ s^{-2} near $z = -15$ cm) and stretching (where $\Delta N^2 \simeq -0.16$ s^{-2} near $z = -4$ cm) of isopycnal layers. Conversely, downstream of the barrier the isopycnal layers are stretched and compressed at $z = -15$ cm and

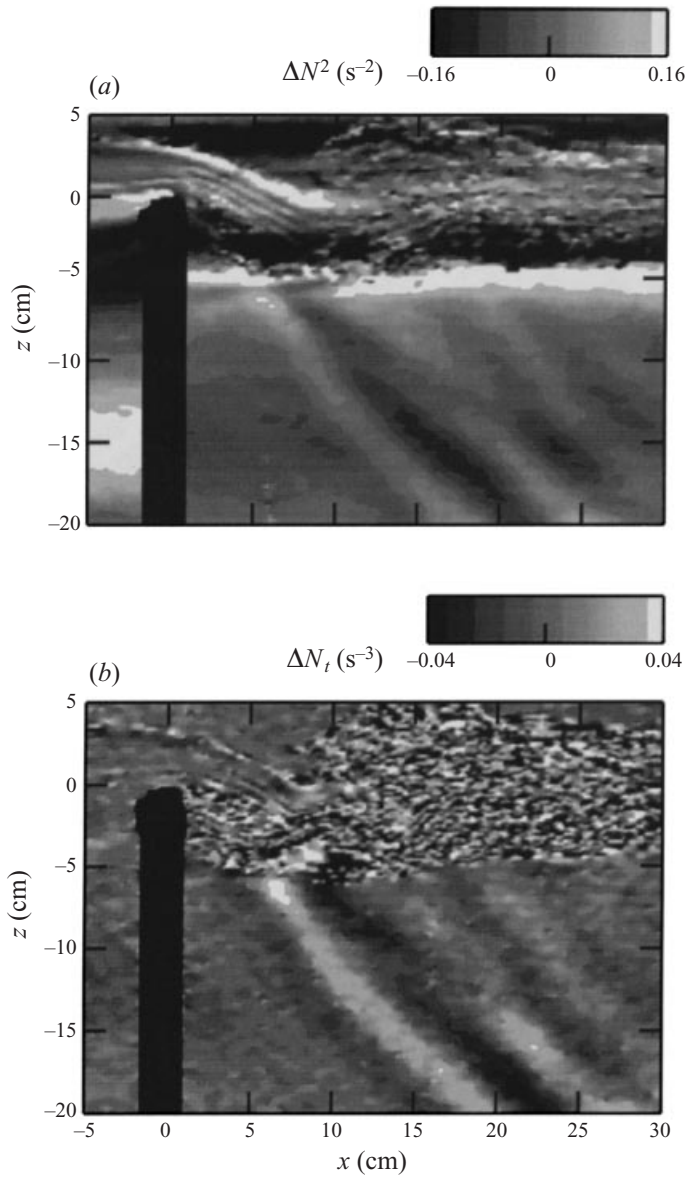

FIGURE 2. (*a*) The change in squared buoyancy frequency ΔN^2 and (*b*) its time derivative N_t^2 calculated in Experiment B see text) when IGW are generated downstream of the barrier (at $x = 0$). Note the calculated values are valid only where the flow is approximately spanwise uniform, i.e. not in the turbulent mixing region.

$z = -4$ cm, respectively. In time these maxima propagate upward over many minutes, consistent with the behaviour of IGW with long horizontal extent. As such, these long horizontal IGW are resonant modes whose structure depends upon the geometry of the tank, the position of the barrier in the test section, and the density structure at depths below the top of the barrier. The waves occur well below the top of the barrier where no background flow is forced by the pumping mechanism of the motor. There is no mean flow at these depths to block, and therefore these waves must result

from the shear-induced stress near the surface. Although the study of these waves certainly merits future study, their analysis is beyond the scope of the present work. Because they propagate on long time scales, they are effectively filtered by taking the time derivative. Thus only IGW of frequencies close to the buoyancy frequency are apparent in the N_t^2 field, and most of our analyses are performed on this field.

Although the N_t^2 field is not a useful quantity on its own, velocity fields may be determined from it to within a set of integration constants. Assuming incompressibility, linearity, and supposing that the initial N^2 profile varies slowly on the scale of the vertical wavelength of the IGW, then

$$\partial w'/\partial z = -\partial u'/\partial x \simeq N_t^2/N^2. \tag{2.3}$$

The linearity assumption requires some clarification. It will be shown that the amplitude of vertical displacements due to IGW well below the mixing region is less than 1 mm, which is small compared with horizontal wavelengths of the order 7 cm. This does not contradict our claim that nonlinear effects are relevant to interactions between radiating IGW and the mean flow. As we will show, the amplitude of IGW at the base of the mixing region where they are generated is a significant fraction of the wavelength.

The vertical velocity field can be determined from equation (2.3) by vertically integrating the field N_t^2/N^2, the result being determined to within an integration constant $C(x)$ for each horizontal position x of a row of pixels. Likewise, the horizontal velocity field can be found by horizontally integrating equation (2.3), and the fluctuation density and vertical displacement field can be determined to within a set of integration constants from the field of ΔN^2.

When integrating in practice, cumulative noise (for example, due to variations in air temperature or degradation of images stored for long times on video tape) can overwhelm the signal from the IGW field.

IGW wavenumbers and frequencies are found from power spectra of space–time plots of the N_t^2 field. We find, in general, that the spectra of IGW generated by instabilities are sharply peaked about a narrow range of values. The peak value itself can be used to determine the IGW amplitude for waves of a particular frequency and wavenumber by using a technique adapted from Alexander (1996). This method, which uses a wavelet analysis to determine the spatial and temporal extent of the wavepacket, is described in detail in §4.

3. Results

Depending on the motor speed (and also weakly depending on the degree of stratification) the near surface fluid upstream of the barrier accelerates to speeds between 0.5 cm s^{-1} and 2.5 cm s^{-1} approximately 60 s after the motor is turned on. Once established the flow speed is uniform in the vertical over the top 6 cm. Over many minutes mixing downstream tends to decelerate the flow near the surface and the upstream velocity profile gradually evolves in response. The fluid over the bottom 20 cm is stationary throughout each experiment except for fluctuations due to IGW. A detailed understanding of the mixing region dynamics, though interesting, is beyond the focus of the present study. Instead we examine the flow immediately downstream of the barrier, studying the development of coherent structures in the lee and how these couple with radiating IGW.

Figure 3 shows a schematic of the flow typically observed in the mixing region. The lee wave that develops downstream of the barrier occurs on a scale U/N_{mix},

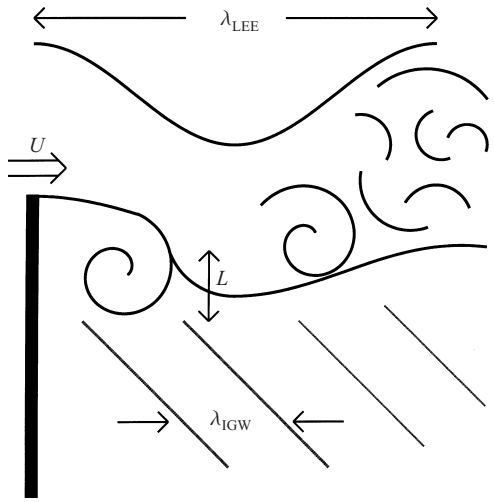

FIGURE 3. A schematic of the typical structure of the flow downstream of the barrier. The indicated length scale, L, and velocity scale U, are those relevant to the generation of IGW (of wavelength λ_{IGW}) by vortices shed in the wake of the barrier. IGW excitation is distinct from the excitation of lee waves (of wavelength λ_{LEE}), which develop on a scale U/N in which N is a characteristic value of the buoyancy frequency in the mixing region.

in which U and N_{mix} are characteristic values of velocity and initial background buoyancy frequency, respectively, determined near the depth of the top of the barrier. Instabilities in the lee occur on a smaller scale, these being determined by the thickness of the shear on the lower flank of the flow (see, for example, figure 2). Precisely what determines this scale is not well understood although, from Miles (1968), unstable flow is expected to occur on scales smaller than U/N_{mix}. We estimate this length scale L in experiments to be the extent of the turbulent fluid at the base of the mixing region at a distance downstream where the mixing region is deepest, as indicated schematically in figure 3. The velocity scale U is defined to be the flow speed at the top of the turbulent fluid.

Typical characteristic scales are $L \simeq 1$ cm and $U \simeq 0.5$ cm s^{-1}. These values are consistent with the length and time scales of radiating IGW, which have wavenumbers on the order of $k_x \simeq 1$ rad cm^{-1} and frequencies on the order of $\omega \simeq 0.5$ rad s^{-1}. The corresponding Reynolds number for most experiments examined in detail here is $Re \simeq 50$.

Although the typical Reynolds numbers are small, the time-scale for viscous diffusion of IGW is $\tau_v = 1/(\nu k_x^2) \simeq 100$ s, an order of magnitude larger than the wave period. Therefore, for most purposes, viscous effects upon the wave propagation can be ignored. The structure of the downstream flow evolution depends on the stratification and flow speed, and may be characterized by a buoyancy parameter $J_{mix} = N_{mix}^2/(U/L)^2$. Equivalently, a Froude number, $J_{mix}^{-1/2}$, could be defined, but we work with J_{mix} in order to make a direct analogy to numerical simulations. If $J_{mix} < 1$ the shear flow is less stable to dynamic instability than if $J_{mix} > 1$. Although we examine only a limited range of parameter space, in general we observe the following behaviour for different values of J_{mix} during the initial stages of each experiment. When $J_{mix} \simeq 0$ a recirculating eddy occurs downstream of the barrier extending to the depth at which the deep water stratification becomes significant, and small-scale disturbances superimposed on the eddy are periodically shed from the barrier. When

$0 < J_{\rm mix} \lesssim 1$ spanwise vortices superimposed on a lee wave are shed quasi-periodically from the barrier (as illustrated in figure 3). Finally, when $J_{\rm mix} \gtrsim 1$ a lee wave develops with transient small-scale disturbances superimposed on it.

In all cases IGW are observed to radiate into the deep fluid as the flow first becomes established, their excitation being directly coupled with the development of spanwise-coherent structures in the lee of the barrier that quasi-periodically deform the base of the mixing region. The amplitude and duration of the wave excitation depends upon the evolution of the mixing region and the degree of stratification of deep fluid. The latter is characterized by a buoyancy parameter $J_{\rm deep} = N_{\rm deep}^2/(U/L)^2$, in which $N_{\rm deep}$ is a characteristic value of the buoyancy frequency in the deep fluid. Thus internal waves of frequency less than $N_{\rm deep}$ may by generated as a consequence of instabilities in the mixing region (on a time scale $\mathscr{L}/\mathscr{U}$), if $J_{\rm deep} > 1$. For a parallel shear flow, linear theory and numerical simulations suggest that weak IGW radiation is expected to occur if the fluid is uniformly stratified, and that strong radiation occurs if $J_{\rm mix} < 0.25$ and $J_{\rm deep} > 0.25$ (Lindzen 1974; Sutherland *et al.* 1994; Sutherland 1996). For the non-parallel flow in our experiments, we expect a similar condition will hold provided the length scale of horizontal variations of the background flow (i.e. the wavelength of the lee wave) is long compared with the depth of the shear flow. For the experiments examined in detail here, we show that this is indeed the case. Although the experiments explore only a limited range of parameter space, the results are consistent with the analytic and numerical predictions.

3.1. *Flow structure*

Figure 4 illustrates the downstream flow 110 s after the motor is turned on for three experiments in which the motor speed and the deep stratification are the same but the stratification of the mixing region is different. We present detailed analyses of these three experiments, in particular, because they most clearly illustrate the dynamics of interest. Each panel shows the initial background squared buoyancy frequency profile $N^2(z)$ to the left of processed images of the N_t^2 field on a grey scale ranging from -0.04 to 0.04 $\rm s^{-3}$. The profiles and fields are shown from 5 cm above the top of the barrier to 10 cm below it, and to a distance 25 cm downstream of the barrier which is situated at $x = 0$. The calculation used to determine this field is not necessarily valid in the mixing region where density gradients may be large and spanwise incoherent, although the values may be taken as quantitatively correct in the deep fluid. Nonetheless, the enhanced image conveniently illustrates the coupling of IGW to coherent structures in the mixing region. That is, internal waves are observed to propagate with the same length scale and horizontal phase speed as disturbances at the base of the mixing region. This is more apparent in continuously moving video images of the flow.

Figure 4(*a*) shows the development of a long lee wave of approximately 15 cm wavelength and the excitation of IGW from the base of the mixing region of approximately 5 cm wavelength. The waves propagate downward and to the right, while the crests of the waves propagate upward and to the right. Hereafter, this experiment is denoted Experiment A. Figure 4(*b*) shows the downstream flow in an experiment, denoted Experiment B, where the stratification is greater near the top of the barrier. In this case $U/N_{\rm mix}$ is smaller and, correspondingly, the wavelength of the lee waves is smaller. Larger vertical structures are also present in the mixing region. In this experiment, large-amplitude IGW are generated over many wave periods even after the mixing region becomes more turbulently developed. Figure 4(*c*) shows the downstream flow in an experiment, denoted Experiment C, in which the stratification of the mixing region is larger still, and the excitation of IGW is relatively weak. In this

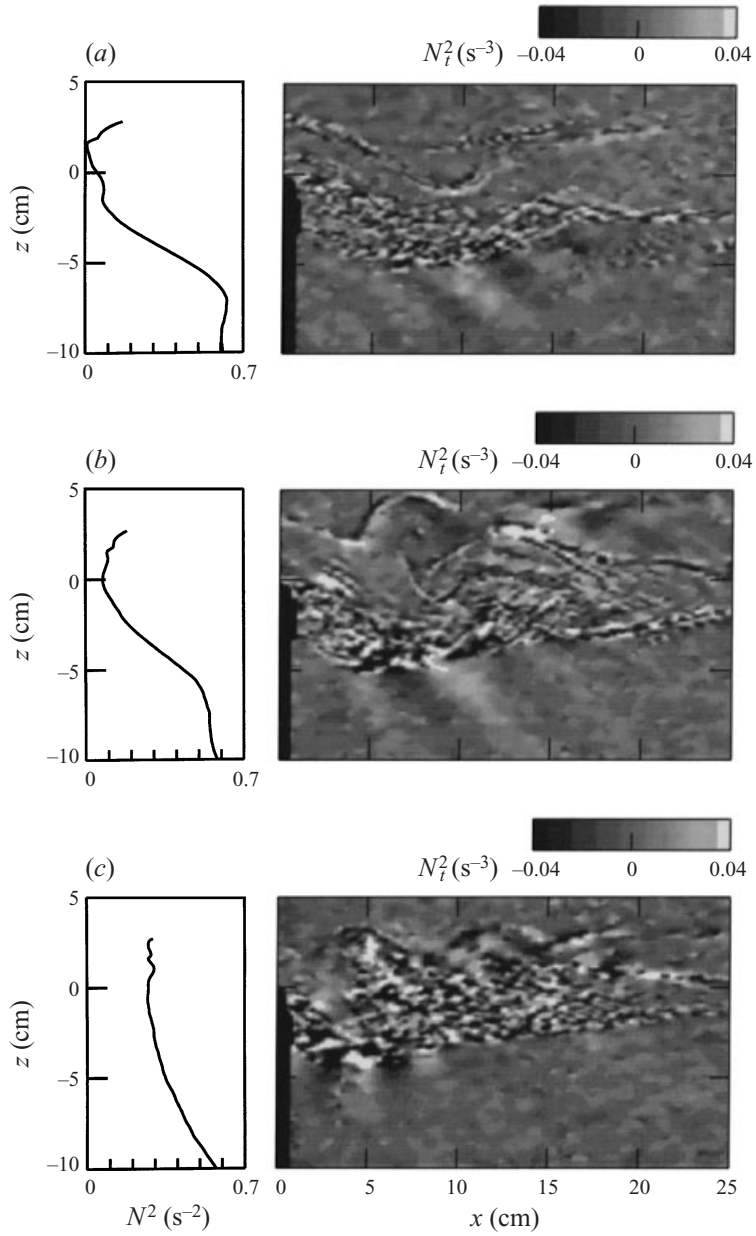

FIGURE 4. Initial N^2 profiles (left-hand panels) and the N_t^2 field (right-hand panels) for three experiments: (*a*) Experiment A, (*b*) Experiment B, and (*c*) Experiment C. The N_t^2 fields are shown from 5 cm above to 10 cm below the barrier and to 25 cm downstream of the barrier. The scale ranges from black to white for values of N_t^2 from -0.04 to 0.04 s^{-3}. In all three experiments the motor speed is the same and the images shown are taken 110 s after the motor is turned on.

case IGW are excited with frequency comparable to the buoyancy frequency of the deep fluid. At later times, however, as the mixing region becomes well mixed, it will be shown that bursts of large-amplitude IGW may nonetheless occur.

Quantitative data summarizing the salient results of Experiments A, B and C are listed in table 1. The table entries are explained in detail in the next section. We

	Expt A	Expt B	Expt C
L (cm)	1.0	1.1	1.3
U (cm s^{-1})	0.61	0.64	0.39
J_{mix}	0.13	0.23	3.0
J_{deep}	1.8	1.9	7.2
λ_x (cm)	7.7	7.7	7.7
T (s)	15.0	10.8	11.7
$\Theta = \cos^{-1}(\omega/N_{\mathrm{deep}})$	59.9°	45.9°	50.1°
X_w (cm)	10.7	11.1	12.0
T_w (s)	83.2	48.2	58.9
$A_{N_t^2}$ (s^{-3})	0.003	0.018	0.003
A_u (cm s^{-1})	0.005	0.032	0.004
A_w (cm s^{-1})	0.003	0.031	0.004
A_z (cm)	0.002	0.026	0.003
$\langle u'w' \rangle$ (10^{-4} cm ^{2} s^2)	−0.08	−5.0	−0.08
$2\lvert\Delta\langle u\rangle\rvert/U$%	0.2	7	0.2

TABLE 1. IGW characteristics, amplitudes, and wavepacket extents determined in three experiments from horizontal time series of the $N_t^2(x,t)$ field at a depth 10 cm below the top of the barrier (see text). Our estimation of the impact of IGW excitation back upon the mean flow is based upon data in the last row of the table. This gives the percent change to the average mean flow over the depth of the shear which decelerates over the horizontal extent of the IGW wavepacket due to momentum transport away from the mixing region.

note here that the characteristic velocity and length scales in the mixing region $\mathscr{U}$ and $\mathscr{L}$, respectively, are sufficiently large that viscous effects can be neglected. The Reynolds numbers of the flows range from approximately 400 to 600. Consistent with observations and measurements of Experiments A, B and C, vortex shedding occurs when $J_{\mathrm{mix}} < 1$ and large-amplitude internal wave excitation occurs when the fluid below the mixing region is sufficiently strongly stratified, $J_{\mathrm{deep}} > 1$.

3.2. *IGW excitation*

IGW are generated due to vertical motions at the base of the mixing region and are regular over many wave periods suggesting that they are coupled directly to coherent structures in the mixing region. This is clear from video images, but can be adequately demonstrated by showing time series of vertical cross-sections of the flow. Figure 5 shows the filtered N_t^2 field for the same three experiments shown in figure 4 but for vertical cross-sections of the flow 7.5 cm downstream of the barrier between 60 and 160 s after the motor is turned on the cross-section extending from 5 cm above the top of the barrier to 15 cm below it. In all three experiments the phase lines move upward in time, behaviour consistent with downward propagating IGW. The slope of the phase lines is the vertical phase velocity and the distance between the crests of the waves gives the period. Figure 5(*a*) shows IGW are excited as soon as mixing begins downstream of the barrier ($t \simeq 90$ s). The relatively weak waves are excited for approximately 3 wave periods. Afterwards, wave excitation still occurs though it is substantially weaker. In comparison figure 5(*b*) shows that relatively strong IGW excitation occurs in Experiment B, for which the stratification in the mixing region is moderately larger. Note that in this panel the grey scale is shown for values spanning a greater range: $|N_t^2| \leqslant 0.06$ s^{-3}. Long period IGW occur as mixing begins after

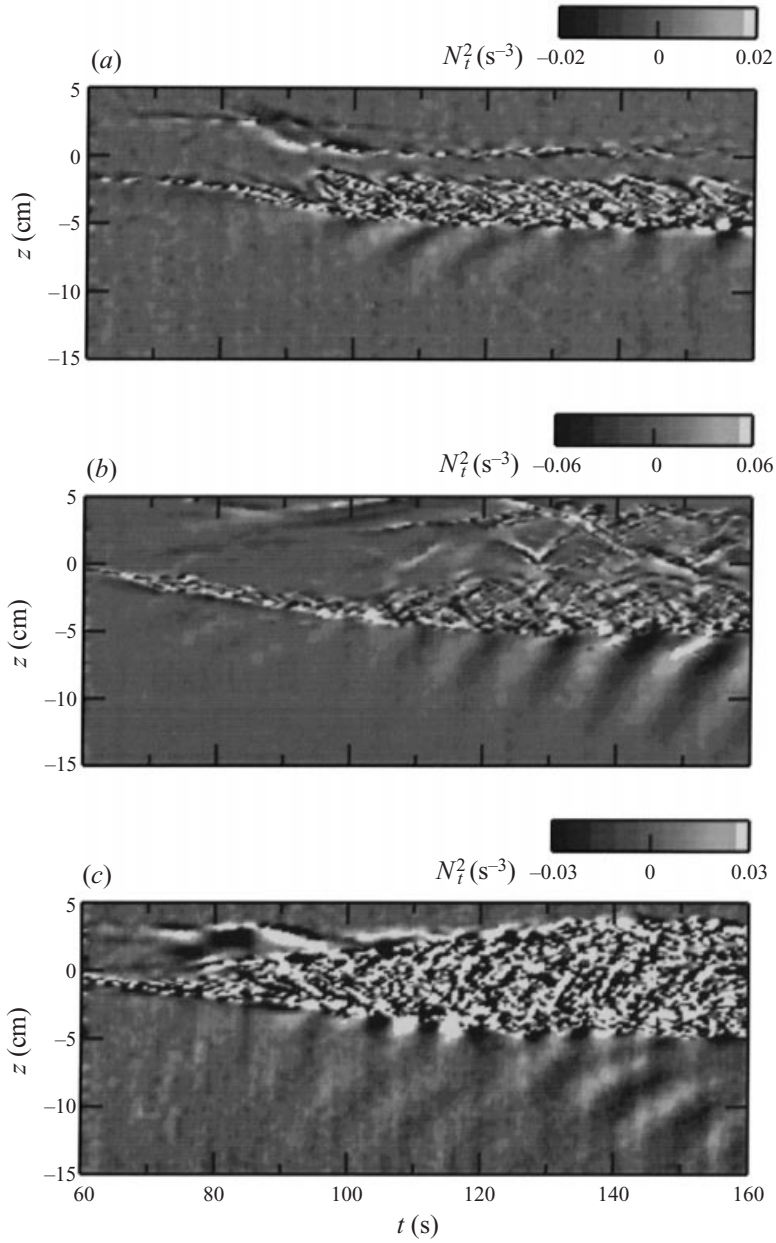

FIGURE 5. Vertical time series of the N_t^2 field for the same three experiments shown in figure 4: (*a*) Experiment A, (*b*) Experiment B, and (*c*) Experiment C. The time series are shown of a vertical cross-section of the flow 7.5 cm downstream of the barrier from 60 s to 160 s after the motor is turned on. The cross-sections extend from 5 cm above the top of the barrier to 15 cm below it. The ranges of the grey scales are different as indicated in the top right corner of each diagram.

between 60 and 90 s, although they are initially weak. Very large amplitude IGW of frequency close to the buoyancy frequency are excited after 100 s when large coherent structures are periodically shed in the wake of the barrier. If the initial stratification in the mixing region is greater still, as shown in figure 5(*c*) for Experiment C, coherent

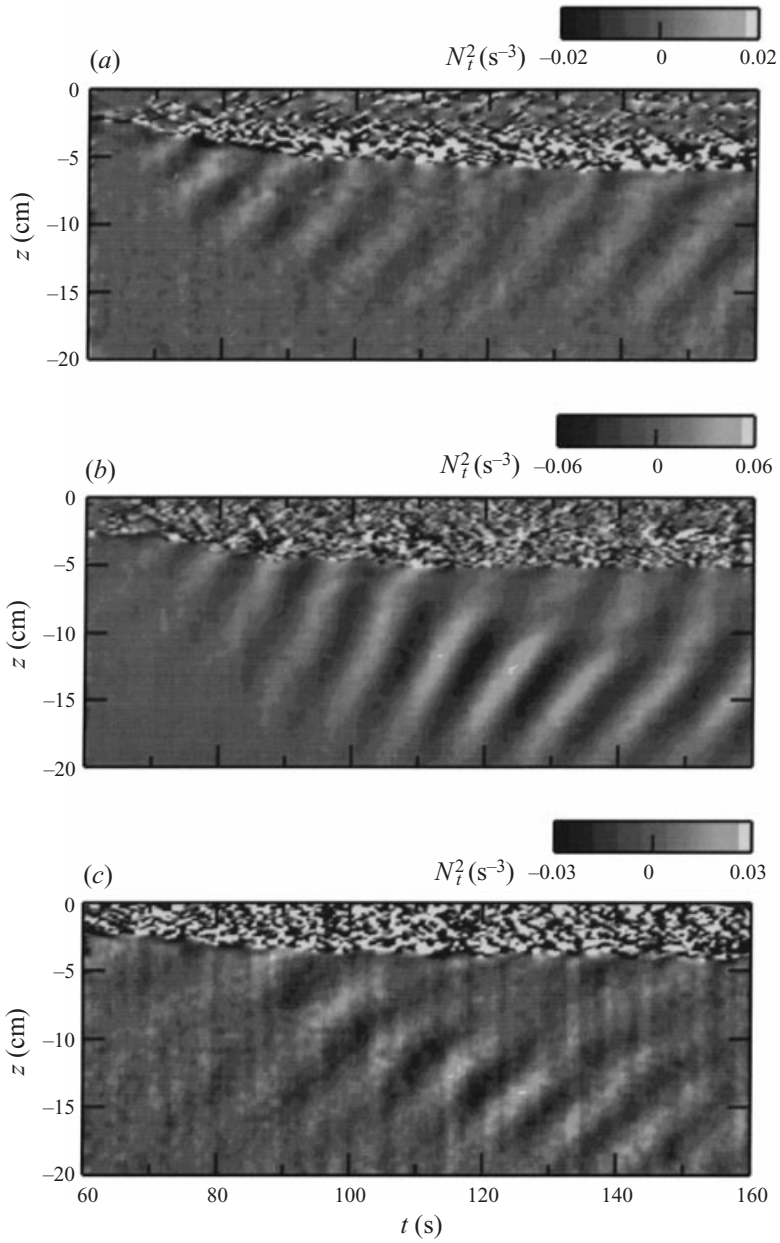

FIGURE 6. Vertical time series of the N_t^2 field as in figure 5 but for a vertical cross-section 15 cm downstream of the barrier shown from 100 s to 200 s after the motor is turned on, and extending from the top of the barrier to 20 cm below it.

structures in the wake of the barrier are shed at frequencies greater than the buoyancy period. The base of the mixing region is strongly perturbed between 100 and 120 s but propagating IGW are not excited. At later times weak IGW excitation occurs for waves of smaller frequency.

For the same three experiments, the behaviour of the waves further downstream is demonstrated in figure 6, which shows a time series of the N_t^2 field for a vertical slice

15 cm downstream of the barrier. The fields are shown for times from 100 to 200 s after the motor is turned on and at depths between the top of the barrier and 20 cm below it. In each case, even though the mixing region at this distance downstream of the barrier is spanwise incoherent, IGW wavepackets generated at the base of the mixing region continue to be excited, propagating downward while the phase lines move upward. Figure 6(*a*) shows that weak IGW wavepackets are excited transiently, the waves occurring in bursts between 110 and 150 s and again after 170 s. The waves that occur in Experiment B, as shown in figure 6(*b*), are excited continuously once they are generated after 110 s, although their frequency and vertical phase speed decreases somewhat in time. The waves are directly excited from the mixing region until 150 s after which time the excitation is weaker near the base of the mixing region and the peak amplitudes occur at depths between 10 and 15 cm. Note that the grey scale is shown in this experiment for $|N_t^2| \leqslant 0.06$ s^{-3}. Figure 6(*c*) shows the propagation of a wavepacket well below the mixing region in Experiment C. In this case, coherent structures 15 cm downstream of the barrier excite IGW between 120 to 140 s. At later times IGW of approximately half the amplitude and longer period are excited.

In summary, instabilities in the lee of the barrier lead to quasi-periodic deformations of the base of the mixing region. When the mixing region initially is weakly stratified the frequency at which the deformations occur is sufficiently small to excite IGW in the deep fluid. When the mixing region is more strongly stratified the base of the mixing region deforms at a greater frequency and IGW are excited by superharmonics and smaller structures that evolve on slower time scales in the well developed flow.

3.3. *Long time behaviour*

Mixing downstream of the barrier acts in time to reduce substantially the stratification in the mixing region. For example, figure 7(*a*) shows successive profiles of $N^2(z)$ in Experiment C, determined from periodic traverses of a conductivity probe 35 cm downstream of the barrier. The light vertical dashed lines in the diagram indicate where $N^2 = 0$ for each profile. The first profile is taken 60 s after the motor is turned on and profiles are taken approximately every 56 s thereafter. The seventh profile taken at 397 s and the fifteenth profile taken 848 s after the motor is turned on are explicitly indicated for comparison with figures 7(*b*) and (*c*). A single traverse is taken over 3 s at a sampling rate of 100 Hz. The profiles show the development of a strong thermocline after approximately 350 s at a depth approximately 3 cm below the top of the barrier. In time, the stratification of the thermocline increases as its depth increases 2 cm during the course of the experiment. As the thermocline becomes more strongly stratified, it deepens on average at a slower rate. The density profile in the mixing region varies greatly between measurements but, over all, the stratification is reduced between 1 and 3 cm depth. The measurements are taken sufficiently far downstream that the turbulence has almost fully collapsed in the sense that the flow is statically stable almost everywhere, and the N^2 profiles exhibit spatial variations no smaller than 1 cm (an order of magnitude larger than the probe resolution).

The thermocline development is consistent with the results of mixing box experiments, in which grid-generated turbulence mixes fluid that is initially uniformly stratified (Thorpe 1966; Linden 1975). In particular, Linden explained that the mixing layer should deepen at a power law rate due to the action of the turbulence present at the bottom of the mixing region alone. However, unlike the mixing box experiments, here the source of the turbulence is localized horizontally as well as vertically, and therefore the deepening of the mixing layer should not necessarily follow the same behaviour. Indeed, following the development of the thermocline we observe that the

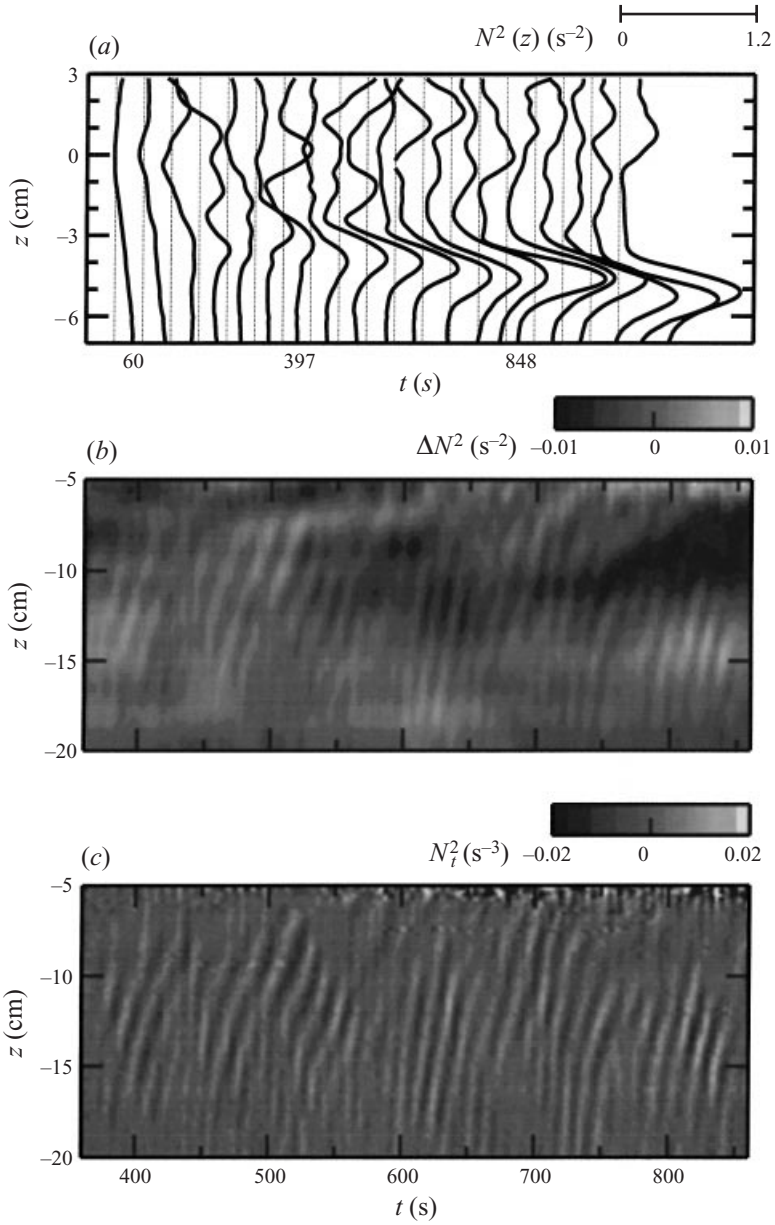

FIGURE 7. For Experiment C: (*a*) successive profiles of N^2 taken every 56 s, 35 cm downstream of the barrier, (*b*) vertical time series of the ΔN^2 field, and (*c*) vertical time series of the N_t^2 field at a position 35 cm downstream of the barrier. The cross-sections extend from 5 to 20 cm below the top of the barrier and are shown between 360 to 860 s after the motor is turned on.

mixing region on average deepens by no more than 1 cm over 20 minutes, and that the depth of the thermocline occasionally decreases (typically by 0.5 cm over several minutes) due to transient unsteady motions in the lee wave and due to wave motions on the scale of the tank itself.

Although the experiments are performed in a recirculating tank, for flow speeds $\simeq 0.5$ cm s^{-1}, the fluid would take $\simeq 1400$ s to travel once around the tank, a time

longer than the duration of a single experiment. Nonetheless, the velocity profile varies on the scale of minutes, which presumably occurs due to large horizontal-scale wave motion propagating upstream of the barrier and downstream from the mixing region. In response to these velocity changes, transient bursts of IGW may occur.

Figures 7(*b*) and (*c*) show time series of the ΔN^2 and N_t^2 fields, respectively. The fields are shown between 360 and 860 s at a distance 15 cm downstream and from 5 to 20 cm below the top of the barrier. To enhance the image, a low pass filter has been applied to each column of figure 7(*b*) to reduce noise that is an artifact of the schlieren grid lines, though some horizontal banding remains. The field shows dominant motion on two time scales. On the short time scale IGW propagate downward with periods of approximately 15 s; on the long time scale wave modes on the depth scale of the tank occur with a period of approximately 200 s. The latter motions are filtered by examining the time derivative of the field N_t^2 that, in figure 7(*c*), resolves a series of IGW wavepackets.

It is interesting to note that in all three experiments and, in particular, at later times in Experiment C, IGW of similar frequency occur. This feature is most striking in figure 7(*c*), in which wavepackets of similar frequency are continually generated even though the stratification of the mixing region changes significantly.

Some implications may be drawn from these observations. It appears that large-amplitude IGW propagate preferentially with frequencies in a limited range. Because linear theory for IGW propagation predicts no such preference, it seems this behaviour is determined by the manner in which the waves are generated: when large-amplitude IGW are excited at frequencies close to the buoyancy frequency of the deep fluid, they act back upon the mixing region in a way that further enhances their excitation. In brief, it might be said that such IGW are not passively, but actively generated. The quantitative evidence presented in §§ 4 and 5 supports this assertion.

3.4. *Weakly stratified deep water*

Though not the main focus of this study, qualitative analyses were performed for experiments run with a faster motor speed (for which we measure $L \simeq 2$ cm and $U \simeq 2.0$ cm s^{-1}) to compare the effects of weak and strong stratification well below the mixing region ($J_{\mathrm{deep}} < 1$ and $J_{\mathrm{deep}} > 1$, respectively). Potassium permanganate dye placed on top of the barrier is used to visualize the flow in the mixing region in these experiments. In general, the dye reveals that the vortices are spanwise coherent over most of the width of the tank and these periodically deform the base of the mixing region for one to two turnover times before they break up turbulently.

Figure 8 shows the results of an experiment in which the flow over the barrier is unstratified with $J_{\mathrm{mix}} \simeq 0$ and the deep water is strongly stratified with $J_{\mathrm{deep}} \simeq 1.5$. The initial N^2 profile is shown in figure 8(*a*). In this case, a recirculating wake develops in the lee of the barrier and, superimposed on it, small-scale vortices are quasi-periodically shed. During the experiment the perturbation density at the base of the mixing region and of waves in the deep fluid is measured using a conductivity probe. The probe is situated 14 cm downstream and continuously measures the conductivity for one minute at successive levels 2.5, 7.5, 12.5 and 17.5 cm below the top of the barrier. This method does not reveal information about the structure or evolution of IGW but does measure their amplitude and frequency which can be compared with dye-visualization and synthetic schlieren images. Figure 8(*b*) shows the fluid vertical displacement at successive depths determined from conductivity measurements. figure 8(*c*) shows the power spectra determined for each time series. The frequency and width of the spectral peaks with non-zero power, as indicated by

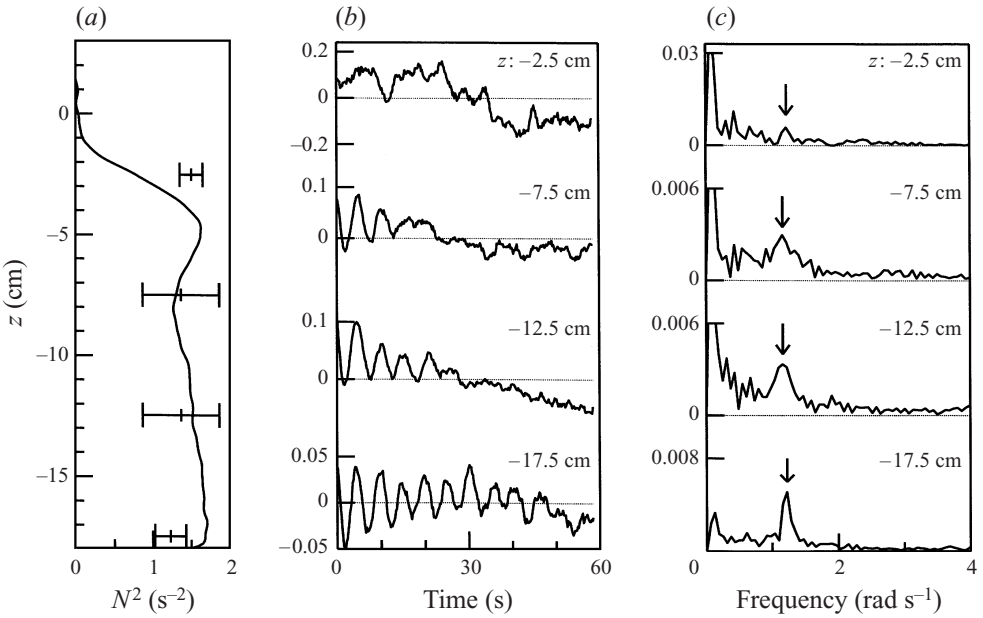

FIGURE 8. (*a*) Initial N^2 profile, (*b*) vertical displacement of fluid due to internal waves at four different depths 2.5, 7.5, 12.5, and 17.5 cm below the top of the barrier, and (*c*) spectra determined from each time series. The error bars in (*a*) are centred about the squared frequency of the peaks indicated by arrows in (*c*), and the width of the error bars are determined from the width of the peaks.

the arrows, are used to compare the squared frequency of IGW with the background squared buoyancy frequency, which are shown in figure 8(*a*) as error bars at the respective depths of each measurement. In this case, although the peak frequency of disturbances at the base of the mixing region is greater than the local buoyancy frequency, IGW with a narrow range of frequencies propagate in the deep water. At each depth, and for all times of the measurements the frequency of the waves is found to be close the buoyancy frequency.

Figure 9 shows the results of an experiment in which the mixing region is strongly stratified with $J_{\mathrm{mix}} \simeq 1$ and the deep fluid is weakly stratified with $J_{\mathrm{deep}} \simeq 0.5$. As in figure 8, the diagrams show the initial background squared buoyancy frequency, vertical displacements in time at four depths, and power spectra of these displacement records. In this experiment vortices are quasi-periodically shed in the lee of the barrier and vortex pairing frequently occurs. However, the frequency of vortex shedding is greater than the buoyancy frequency N_{deep} of the deep fluid, and therefore IGW of the same frequency as the disturbances in the mixing region cannot propagate downward. Nonetheless, as shown in figure 9(*c*), IGW of approximately half the forcing frequency propagate below the mixing region into the deep fluid. The frequency of the waves in the deep fluid, which are presumably subharmonically generated, is again comparable to the buoyancy frequency.

4. Quantitative analysis

Although the conditions under which IGW are generated varies greatly, in general we observe that IGW occur within a limited range of frequencies close to the

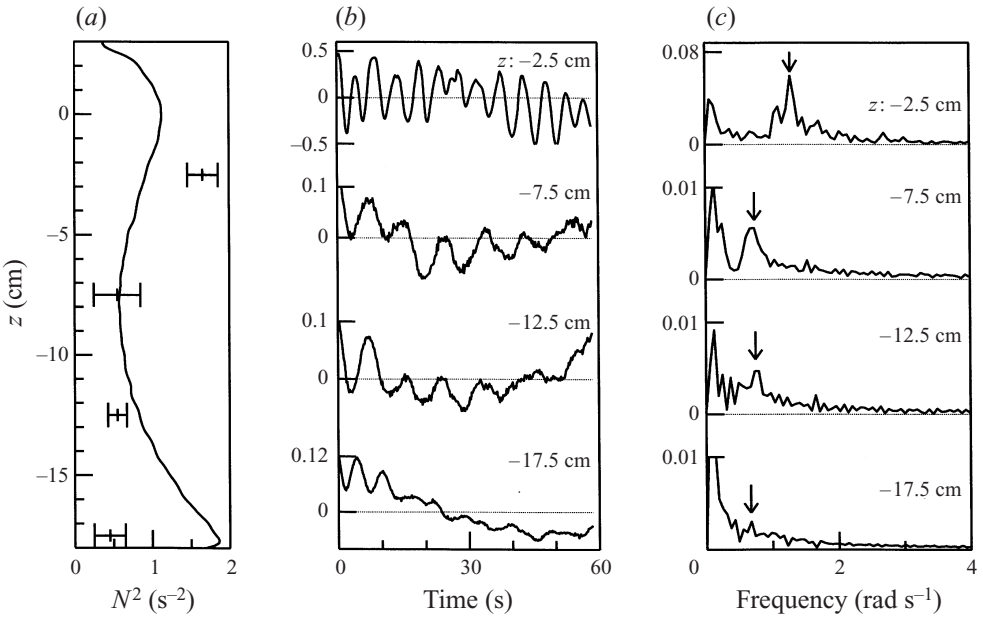

FIGURE 9. As in figure 8: (*a*) the initial N^2 profile, (*b*) vertical displacement in time at the same four depths and (*c*) corresponding spectral peaks. In this experiment, IGW at the base of the mixing region have frequency larger than the buoyancy frequency of the deep fluid. Nonetheless, IGW of half the frequency propagate downward.

buoyancy frequency of the fluid below the mixing region. A measure of the frequency and horizontal wavelengths of IGW is given by constructing space–time plots from a horizontal cross-section of the N_t^2 field at a fixed depth below the mixing region. For example, figure 10(*a*) shows this field over 150 s beginning 100 s after the motor is turned on in Experiment B. The cross-section is taken at a level 10 cm below the top of the barrier between 4 and 27 cm downstream. Figure 10(*b*) shows the power spectrum of this field, as determined from the squared discrete Fourier coefficients $|\mathscr{F}_{k_x\omega}|^2$. The figure demonstrates that most of the energy of the wavepacket is concentrated in a narrow band of wavenumbers and frequencies.

Such time series are constructed for Experiments A, B, and C, the qualitative behaviour which was discussed in detail in §3. The first four rows of table 1 list the relevant parameters of each experiment. L and U are length and velocity scales, respectively, characterising the shear depth at the base of the mixing region. J_{mix} and J_{deep} are buoyancy parameters characterising the stratification in the mixing region and deep fluid, respectively. The wavelength and period of IGW are determined from the horizontal time series such as that shown in figures 10(*a*). The IGW characteristics are given for Fourier modes corresponding to non-zero $k_x(=2\pi/\lambda_x)$ and $\omega(=2\pi/T)$ with the largest peak power. The phase tilt Θ of the waves with the vertical is calculated from the IGW frequency and buoyancy frequency of the deep fluid. Note that the wavelength of the strongest IGW is $\lambda_x \simeq 7.7$ cm in all three experiments and their period is such that these waves have phase tilt ranging between 45° and 60°.

To estimate the drag upon the mixing region due to IGW excitation, the amplitude as well as the spatial extent and duration of wave emission needs to be measured. To this end, we employ the wavelet analysis developed by Alexander (1996), who

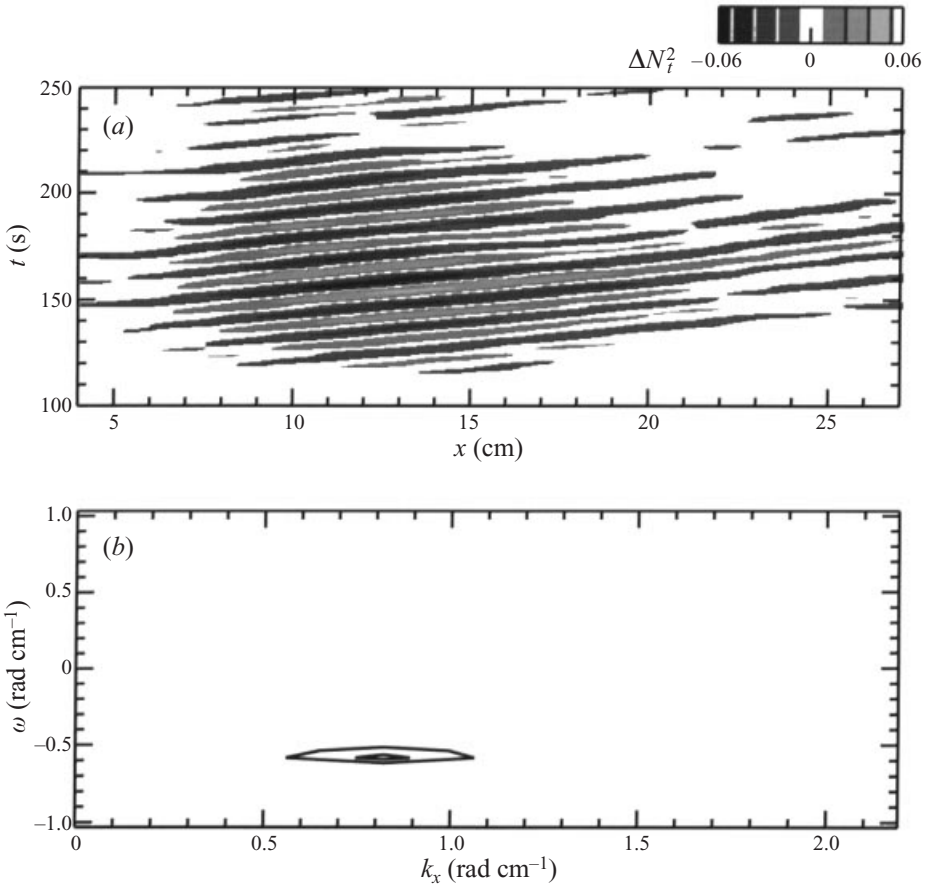

FIGURE 10. Experiment B: (*a*) horizontal time series of the N_t^2 field and (*b*) its power spectrum. The N_t^2 field is shown for a cross-section 10 cm below the top of the barrier from 4 to 27 cm downstream and between 100 and 250 s after the motor is turned on. Grey scale from black to white corresponds to values ranging from −0.06 to 0.06 s^{-3}. Contours 1×10^{-5}.

used this technique to estimate the amplitude of IGW generated by convection in numerical simulations.

In general, for any wavepacket (whether spatially or temporally defined) the amplitude A of waves of a particular spatial frequency k can be estimated from its discrete Fourier transform, $\mathscr{F}_k$. If the waves are periodic over the whole domain, the amplitude is $A = 2|\mathscr{F}_k|$. If the wavepacket is compact, however, a multiplicative factor must be introduced which corrects for the way in which Fourier transforms average power over the domain and for bias which spreads power over a broader frequency range. Explicitly, the corrected amplitude is

$$A \simeq 2\mathscr{C}|\mathscr{F}_k|\left(\frac{L_d}{X_w}\right), \tag{4.1}$$

in which L_d is the extent of the domain, X_w is the width of the wavepacket for waves of frequency k, and the order 1 calibration constant $\mathscr{C}$ that we use for our analyses is determined empirically.

In general, the definition of X_w and $\mathscr{C}$ is somewhat arbitrary. For example, consider a

Gaussian wavepacket defined explicitly by $\exp(-x^2/2\sigma^2)\cos(2\pi x)$, which is composed of waves of wavelength $\lambda_x = 1$ and amplitude $A = 1$. Assuming the wavepacket width is much smaller than the domain size (i.e. $\sigma \ll L_d$), we find that

$$\mathscr{F}_{2\pi} = \frac{\sigma}{L_d}\left(\tfrac{1}{2}\pi\right)^{1/2}[1 + \exp(-8\pi^2\sigma^2)]. \tag{4.2}$$

Putting this in equation (4.1) gives

$$\mathscr{C} = \left((2\pi)^{1/2}\frac{\sigma}{X_w}[1 + \exp(-8\pi^2\sigma^2)]\right)^{-1}. \tag{4.3}$$

The equation shows that the value of $\mathscr{C}$ depends in general upon the wavepacket width X_w. However, as shown below, with a consistent definition of X_w, $\mathscr{C}$ is approximately constant if the width of the wavepacket is much larger than the wavelength (i.e. $\sigma \gg \lambda_x$). In particular, if we set $X_w = \sigma$ in equation (4.3), and we assume $\sigma \gg 1$, then $\mathscr{C} \simeq 1/(2\pi)^{-1/2}$.

For the analytically defined wavepacket in the above example, it is natural to chose $X_w = \sigma$. However, in experiments wavepackets may be composed of waves spanning a broad frequency spectrum, and it is therefore convenient to perform a wavelet analysis in order to estimate the width of the wavepacket enveloping waves of a specific frequency. A wavelet transform is a compromise between a real function, with perfect spatial but no spatial frequency information, and the corresponding Fourier transform, with perfect spatial frequency but no spatial information. For a particular wavelet mode, a wavelet filtered function has non-negligible amplitude only over regions of space where the function has comparable frequency with the mode. We use the Daubechies wavelet filters with 20 coefficients (Press *et al.* 1993).

The width of a particular mode i is defined by

$$L_i = 2(\langle x^2\rangle_{E_i} - \langle x\rangle_{E_i}{}^2)^{1/2}, \tag{4.4}$$

in which the angle brackets denote the domain average weighted by the energy of wavelet mode i. This definition, though different from that used by Alexander (1996), is useful in our study since we find that the wave amplitude is more accurately predicted for a variety of envelope shapes. Finding the energy-weighted least-squares fit line through L_i as a function of the spatial frequency of each mode i, the extent, X_w, of the wavepacket of frequency k is determined.

In order to determine the calibration constant $\mathscr{C}$, the widths and amplitudes of analytically defined wavepackets are calculated using equations (4.1) and (4.4), and the results are compared with the actual amplitude of the waves. Specifically, we examine wavepackets of half-width σ defined by $\exp(-x^2/2\sigma^2)\sin(2\pi x)$, $\exp(-x^2/2\sigma^2)\cos(2\pi x)$, and $H(\sigma - |x|)\sin(2\pi x)$, where $H(x)$ is the Heaviside function: $H(x) = 0$ for $x < 0$; $H(x) = 1$ for $x \geqslant 0$. The functions are defined at a discrete set of 512 points, with x ranging from -10 and 10, although the results are not sensitive to these values provided the waves are sufficiently well resolved. The third and fourth columns of table 2 show the calculated values of X_w and $2|\mathscr{F}_{2\pi}|$, respectively. Substituting these values in equation (4.1) gives values of $\mathscr{C}$, which are found to be approximately constant if $\lambda_x \ll \sigma \ll L_d$. Based on this information, to determine the amplitude of the wavepackets observed in experiments, we set $\mathscr{C} = 0.59$ as our calibration constant in equation (4.1). As a check on the accuracy of this choice, the amplitudes of the three types of analytically defined wavepackets are calculated and compared with the correct value of 1. The results, which are listed in the fifth column of table 2, show that the amplitudes are correctly predicted to within 3% of their actual value

Wavepacket definition	σ	X_w	$2\,\lvert\mathscr{F}_{2\pi}\rvert$	A
$H(\sigma - \lvert x\rvert)\sin 2\pi x$	1	1.66	0.1	0.719
	2	2.57	0.2	0.918
	4	4.61	0.4	1.024
	6	7.05	0.6	1.005
$\exp(-x^2/2\sigma^2)\sin 2\pi x$	1	2.44	0.13	0.605
	2	3.28	0.25	0.902
	4	5.80	0.50	1.008
	6	7.99	0.68	1.004
$\exp(-x^2/2\sigma^2)\cos 2\pi x$	1	2.04	0.13	0.726
	2	3.09	0.25	0.958
	4	5.81	0.50	1.006
	6	7.93	0.68	1.011

TABLE 2. Results of wavelet analysis of analytically defined wavepackets of half-width σ composed of waves of (spatial) frequency 2π and amplitude 1 (see text). The wavepacket width calculated by a wavelet analysis is X_w. For plane IGW of period 2π, $2|\mathscr{F}_{2\pi}|$ is the correct IGW amplitude in terms of the discrete Fourier coefficient $\mathscr{F}_{2\pi}$. For localized wavepackets, an estimate A of the actual wave amplitude is determined in terms of the ratio of X_w to the domain size.

provided the wavepacket envelope is more than five times as large as the wavelength. For envelope widths comparable to the wavelengths, the calculated amplitudes are moderately under-predicted.

In our analysis of experimentally generated IGW, we simultaneously determine the spatial and temporal extent of a horizontal time series of the N_t^2 field. For Experiments A, B and C, the calculated horizontal extent X_w and duration T_w of IGW wavepackets determined according to (4.4) are given in table 1. The peak of the power spectrum of the N_t^2 field gives the wavenumber k_x and ω of the waves, and the corrected amplitude of the (k_x, ω) mode is

$$A_{N_t^2} \simeq \frac{1}{2}\mathscr{C}^2 |\mathscr{F}_{k_x\omega}| \left(\frac{L_x L_t}{X_w T_w}\right), \tag{4.5}$$

in which L_x (L_t) is the spatial (temporal) extent of the domain.

Only a small number of wavelet modes of the spatio–temporal fields have a component with significant energy. For example, applying the wavelet transform to the field shown in figure 10(*a*), it is found that 66% of the total energy of the field is contained in the particular wavelet mode shown in figure 11.

From linear theory, amplitudes of other fluctuation quantities can be determined from $A_{N_t^2}$. For monochromatic IGW described by the streamfunction $\psi = A\cos(\boldsymbol{k}\cdot\boldsymbol{x} - \omega t) = A\cos\phi$,

$$N_t^2 = N^2 k_x k_z A\cos\phi + \frac{\mathrm{d}N^2}{\mathrm{d}z} k_x A \sin\phi. \tag{4.6}$$

If $N^2(z)$ varies sufficiently gradually with z, the second term can be ignored. The amplitudes of the horizontal velocity (A_u), vertical velocity (A_w), and vertical displacement (A_z), in terms of the amplitude $A_{N_t^2}$ of the N_t^2 field are

$$A_u = A_{N_t^2}/(k_x N^2),$$
$$A_w = A_{N_t^2}/(k_x N^2 \tan\Theta),$$

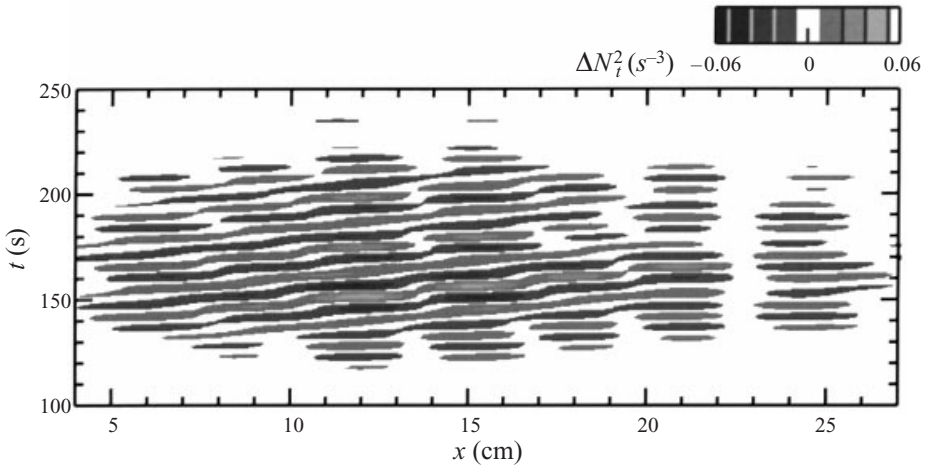

FIGURE 11. The N_t^2 field for the wavelet corresponding to the mode (3,5) containing 66% of the energy of the field shown in figure 10(*a*). The field is shown over the same extent and duration and over the same scale as the original horizontal time series.

$$A_z = A_{N_t^2}\omega/(k_x N^4 \tan\Theta),$$

in which $\Theta = \cos^{-1}(\omega/N)$. Values for these amplitudes are shown in table 1.

As a check on these results, the amplitude of the horizontal velocity field is estimated by observing the horizontal motion of a vertical dye line at a depth 10 cm below the top of the barrier. For example, in Experiment B, dye lines situated approximately 7 cm and 11 cm downstream of the barrier were observed to oscillate with the same frequency as the radiating IGW when strong wave excitation occurred between 100 s and 250 s after the motor was turned on. Because the IGW wavelength is 7.3 cm and the dye lines are separated by almost half that distance, the oscillations of the two lines are approximately 180° out of phase. Typical peak-to-peak horizontal displacement of the lines was $2A_x \simeq 0.2$ cm, as shown in figure 12(*a*). By fitting a cubic spline to these curves and time differentiating, the fluctuation horizontal velocity is determined as shown in figure 12(*b*). The amplitude determined in this way is $A_u = \simeq 0.05$ cm s^{-1}, which is the same order as the value 0.03 cm s^{-1} predicted from the analysis of the N_t^2 fields. The comparison implies that the amplitudes listed in table 1 moderately under-predict the actual values. The discrepancy is attributed to signal filtering and because the horizontal extent of the wavepacket is comparable to the IGW horizontal wavelengths, leading to bias in the wavelet analysis, as discussed above.

The second to last row of table 1 gives the Reynolds stress per unit mass, $\langle u'w'\rangle = -\frac{1}{2}A_u A_w$, which is related to the vertical flux of horizontal momentum across the width X_w of the wavepacket. Integrating this flux in time and assuming IGW are generated over the characteristic length L of the shear flow at the base of the mixing region, an estimate of the local deceleration of the flow due to IGW excitation is given by

$$\langle \Delta u\rangle \simeq \langle u'w'\rangle T_w/L. \tag{4.7}$$

This is given as a percentage of the average flow over the shear depth, $U/2$, in the last row of table 1. Values for the change in flow speed are given as a fraction of the characteristic flow speed. In Experiment B, in particular, the analysis shows that the mean flow over the extent of the wavepacket is decelerated by approximately 7% of its characteristic flow speed over the time of the wavepacket excitation.

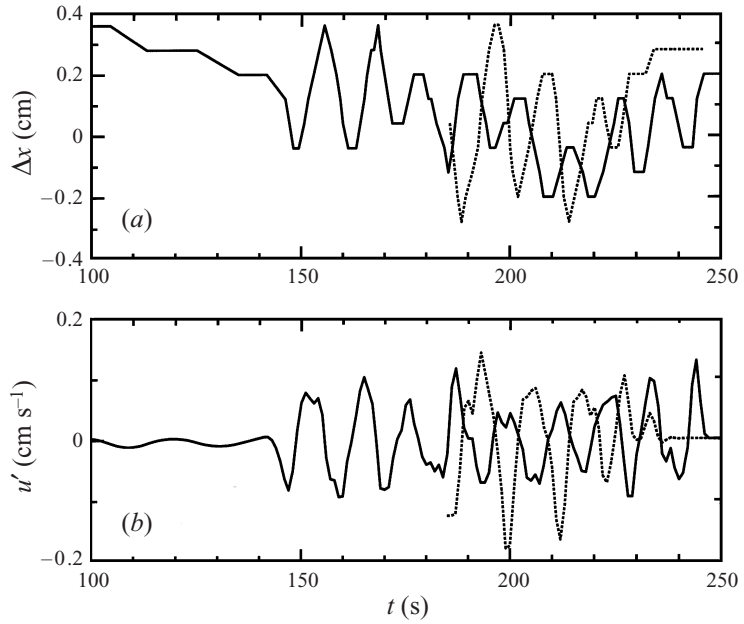

FIGURE 12. Experiment B: (*a*) horizontal displacement of dye lines 7 cm (solid line) and 11 cm (dotted line) downstream of the barrier at a depth 10 cm below the top of the barrier. The second dye line is dropped only 183 s after the motor is turned on. The corresponding horizontal velocity for each dye line is shown in (*b*).

Indeed, in video images of the mean flow over this time, deformations of the base of the mixing region are observed to move initially with the speed of vortices shed from the barrier, but as disturbances grow and radiating IGW increase in amplitude, the behaviour of these deformations appears to be controlled in part by the waves themselves, so that disturbances at the base of the mixing region move more slowly than the speed of coherent structures in the turbulent region above it.

5. Numerical simulations

The experiments suggest that strong IGW excitation, when it occurs, significantly affects the mean flow. We examine this in more detail numerically using a code developed by Smyth & Peltier (1989). Specifically, we solve the primitive equations for two-dimensional Boussinesq flow in terms of the vorticity Ω and fluctuation density ρ:

$$\mathrm{D}\Omega/\mathrm{D}t = -g\rho + F_\Omega(x,z,t) + \nu\nabla^2\Omega, \tag{5.1}$$

$$\mathrm{D}\rho/\mathrm{D}t = (\rho_{00}/g)N^2 w + \kappa\nabla^2\rho. \tag{5.2}$$

Here $\mathrm{D}/\mathrm{D}t$ is the material derivative, F_Ω is an external forcing to the vorticity field, w is the vertical velocity, g is the acceleration due to gravity, and ρ_{00} is a characteristic value of the density. The kinematic viscosity ν is set so that the Reynolds number $Re = \mathscr{U}\mathscr{L}/\nu = 100$, in which $\mathscr{U}$ and $\mathscr{L}$ are characteristic velocity and length scales, respectively. The diffusivity κ is given by setting $\kappa = \nu$. In fact, the diffusivity of salt water is many orders of magnitude lower than the kinematic viscosity, but stability of the numerical integration prohibits more realistic values. Nonetheless, the shear

generation of IGW is relatively insensitive to diffusive effects over the time scales studied, and the dynamics of interest are well represented. The equations are solved in a channel geometry that is horizontally periodic with free-slip upper and lower boundary conditions. The domain itself ranges from $-80\mathscr{L}$ to $40\mathscr{L}$ in the horizontal and from $-30\mathscr{L}$ to $30\mathscr{L}$ in the vertical. The domain is set up so that boundaries do not significantly affect the flow initially and the simulations are terminated when bottom reflection of IGW occurs or effects of the periodic boundaries become significant.

The background horizontal velocity profile, $U(z)$, and buoyancy frequency profile, $N(z)$, are prescribed initially. We set $U = \mathscr{U}\tanh(z/\mathscr{L})$ and $N^2 = (N^2_{\rm mix} + N^2_{\rm deep})/2 + (N^2_{\rm mix} - N^2_{\rm deep})\tanh((z - z_0)/R)/2$, with $z_0 = -5\mathscr{L}$, and $R = 0.5\mathscr{L}$. By analogy with Experiments A, B, and C, $\mathscr{L}$ is the shear half-depth $\simeq 0.5$ cm and $\mathscr{U} \simeq 0.3$ cm s^{-1} is half the velocity difference between the upper and lower regions. These are only estimates, since the length scales in the experiments are determined from the well mixed states, a smaller value of $\mathscr{L}$ being more indicative. For the sake of argument, it is sufficient for the purposes of the illustration here to set $\mathscr{L} = \mathscr{U} = 1$ in arbitrary units. As with the experiments, $N^2_{\rm mix}$ and $N^2_{\rm deep}$ are the buoyancy frequencies in the shear region and deep fluid, respectively. The corresponding non-dimensional buoyancy parameters are defined by $J_{\rm mix} = N^2_{\rm mix}(\mathscr{L}/\mathscr{U})^2$ and $J_{\rm deep} = N^2_{\rm deep}(\mathscr{L}/\mathscr{U})^2$.

Simulations of the growth and development of the most unstable mode to these analytic basic states were studied by Sutherland (1996). Here, rather than superimpose the (horizontally periodic) most unstable normal mode initially, we introduce a locally defined external forcing to the vorticity field about the shear maximum:

$$F_\Omega = f(t)\exp[-(x^2 + z^2)/2]. \tag{5.3}$$

The strength of the forcing is

$$f(t) = \begin{cases} 0.05, & 0 \leqslant t < 20, \\ 0, & t \geqslant 20. \end{cases} \tag{5.4}$$

This forcing is constant until a vortex develops of strength comparable to the background vorticity, after which time the system relaxes.

The initial conditions of the simulations are by no means an adequate model of flow over a thin barrier, except insofar as they demonstrate the interaction between generated internal waves and the mixing region.

As the simulated vortex forms initially, fluid passing to the right above it and to the left beneath it is vertically displaced in a manner similar to flow over topography. Likewise, IGW excitation is expected to occur if the stratification in the far field is sufficiently strong. With $\mathscr{L} = \mathscr{U} = 1$, the forcing frequency is of order 1 and IGW excitation is expected to occur if $N_{\rm deep} \gtrsim 1$ is of this order (e.g. Gill 1982, §6.8).

The results are shown in figure 13 of a simulation in which the initial background stratification is uniform with $J_{\rm mix} = J_{\rm deep} = 0.05$. The plates show the vorticity field of the flow every 20 time units beginning at $t = 20$ when the forcing to the vorticity field about the origin is turned off and the system begins to relax. In each panel only a portion of the full domain is shown, horizontally with $-40 \leqslant x \leqslant 40$ and vertically with $-15 \leqslant z \leqslant 5$. The simulation shows how the initial forcing triggers the flow to become unstable, the centre vortex spawning the development of vortices to either side that in turn spawn other vortices. The separation between the vortices initially is approximately 16, moderately larger than the wavelength of the most unstable mode $\simeq 12.6$. As the flow evolves, the spacing between vortices continues to increase, although the centre vortex remains stationary.

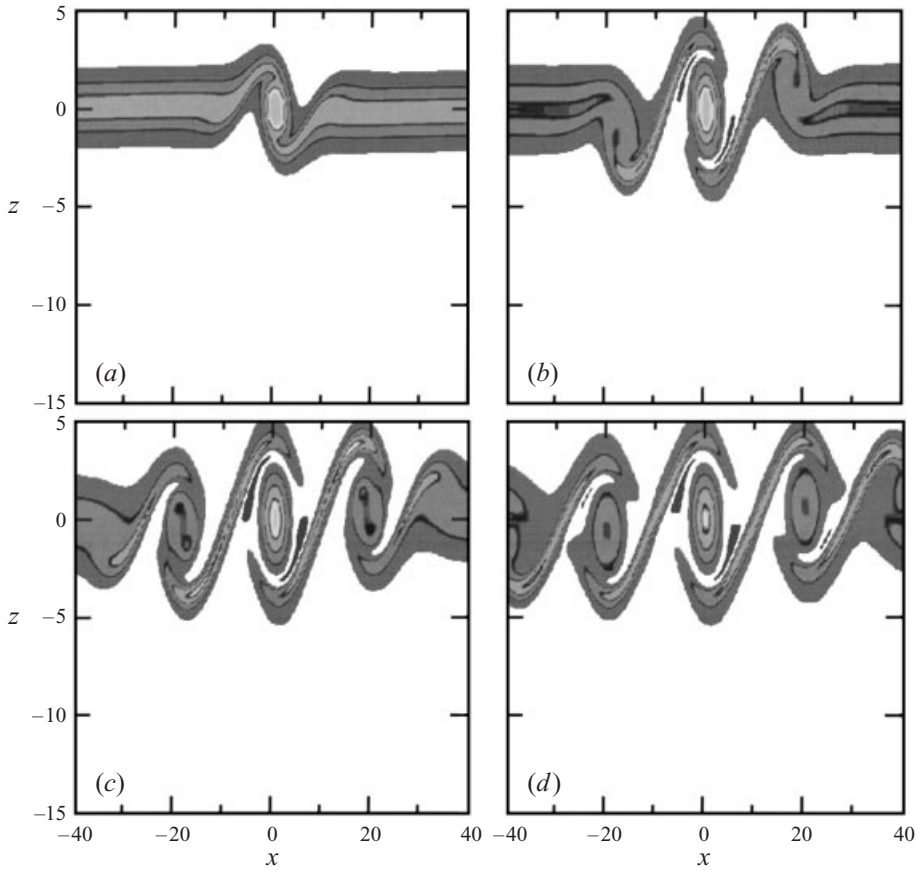

FIGURE 13. The vorticity field shown for numerical simulations of a locally forced uniformly stratified shear flow ($J_{\mathrm{mix}} = J_{\mathrm{deep}} = 0.05$) at times (*a*) 20, (*b*) 40, (*c*) 60, and (*d*) 80.

In comparison, figure 14 shows the results of a simulation with non-uniform stratification. In this case $J_{\mathrm{mix}} = 0.05$ as before but here $J_{\mathrm{deep}} = 1$, sufficiently large that IGW excitation is expected. The panels are shown for the times corresponding to those in figure 13, and the extent of the domain in each plate is the same. The diagrams show that the mixing region itself evolves quite differently when IGW are generated. At time 20 the vortex structure is qualitatively the same as that in the simulation with uniform stratification, although here the development of propagating IGW is apparent beneath the vortex. At time 40 the waves have grown to larger amplitude and extend to a greater depth. Meanwhile, the vortices in the mixing region have developed quite differently from those in the uniformly stratified case. The upstream vortex (with respect to the flow below $z = 0$) is more vertically elongated, the centre vortex is displaced downstream and the downstream vortex is not as intense and less horizontally displaced from the centre vortex. At later times these features become more pronounced. The spacing between the downstream vortices, including the downstream drifting centre vortex, is approximately 13, which is the same as the horizontal wavelength of radiating IGW. The upstream vortices, a distance approximately 20 apart, are separated more widely. On average the centre vortex drifts at about 10% of the speed of the lower leftward flow, an indication of the significant loss of momentum from the mean flow over the horizontal extent of radiating IGW.

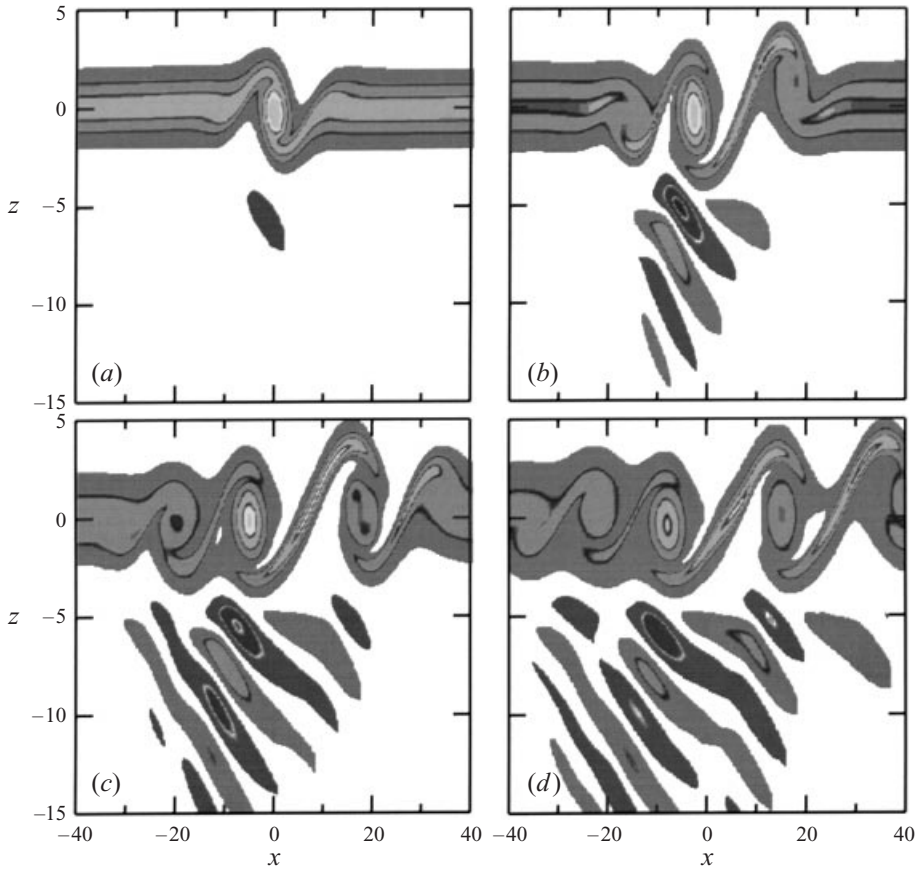

FIGURE 14. The vorticity field shown for numerical simulations of a locally forced non-uniformly stratified shear flow ($J_{\mathrm{mix}} = 0.05$, $J_{\mathrm{deep}} = 1.0$) at times (*a*) 20, (*b*) 40, (*c*) 60, and (*d*) 80.

The flux of momentum from the centre vortex and other vortices as they develop varies depending on the stratification of the deep fluid. Figure 15(*a*) shows the Reynolds stress at $z = -10$ as a function of time for three simulations with $J_{\mathrm{deep}} = 0.05$ (solid line), 0.25 (dotted line), and 1.0 (dashed line). The stratification in the mixing region is characterized by $J_{\mathrm{mix}} = 0.05$ in all three cases. The plots show that momentum is inefficiently transported away from the mixing region if the fluid is uniformly stratified ($J_{\mathrm{mix}} = J_{\mathrm{deep}} = 0.05$), but that significant momentum is carried away from the mixing region by IGW if the deep fluid is moderately more stratified ($J_{\mathrm{deep}} = 0.25$). If the stratification is larger still, the momentum flux decreases to a smaller value.

In the case with $J_{\mathrm{deep}} = 0.25$, the absolute value of the momentum flux per unit mass increases to an approximately constant value of $|\langle u'w' \rangle_{\mathrm{max}}| \simeq 0.008$ after about two buoyancy periods. In analogy with the experiments setting $\mathscr{U} \simeq 0.3$ cm s^{-1} the momentum flux per unit mass is 7×10^{-4} cm^2 s^2, which is of the same order as that for the strongly excited IGW observed in Experiment B.

To quantify the effect of drag due to IGW excitation, the momentum loss in the mixing region is compared with the average momentum of the mean flow over the shear depth. The transport of momentum across $z = -10$ is the integral in time of

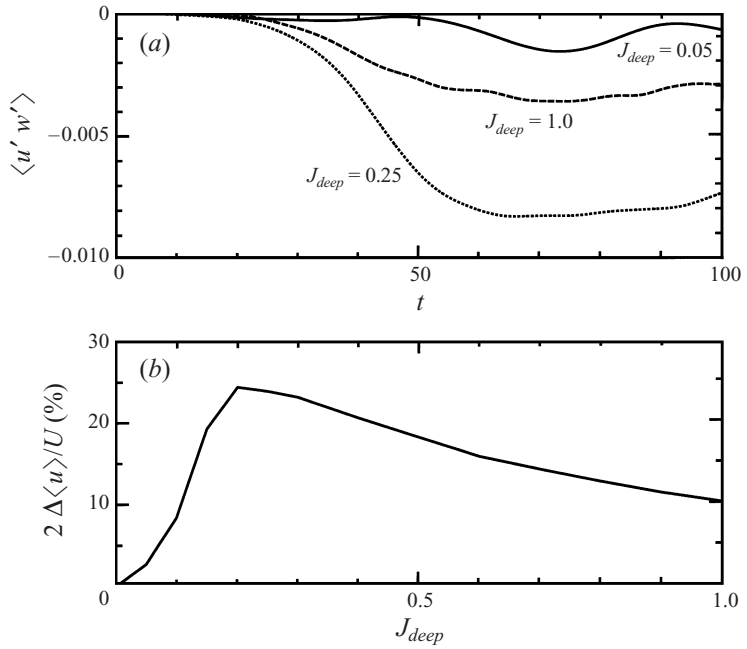

FIGURE 15. (*a*) Reynolds stress in time determined at $z = -10$ in numerical simulations with $J_{\mathrm{mix}} = 0.05$ and $J_{\mathrm{deep}} = 0.05$ (solid line), 0.25 (dotted line), and 1.0 (dashed line). (*b*) As a function of J_{deep}, the estimated percent change to the average mean flow across the shear depth and over the horizontal extent of the simulated IGW wavepackets.

$\langle u'w' \rangle$ at this level. Assuming it is extracted over the shear depth $2\mathscr{L}$ then

$$\langle u \rangle = \int \langle u'w' \rangle \mathrm{d}t / 2\mathscr{L} \tag{5.5}$$

is an estimate of the change in flow speed over the shear depth. Note, this expression differs from equation (4.7) by a factor 2 because $\mathscr{L}$ is a measure of the shear half-depth whereas the experimentally estimated value L is the full shear depth. Figure 15(*b*) compares this change as a percentage of the average flow speed over the shear depth, $\mathscr{U}$, calculated for simulations performed with a range of values of J_{deep} and with $J_{\mathrm{mix}} = 0.05$. The graph shows that up to 25% of the momentum is extracted from the mean flow over the horizontal extent of the radiating IGW wavepacket when $J_{\mathrm{deep}} = 0.2$. For successively larger values of J_{deep} the relative loss of momentum decreases monotonically, being approximately 10% for $J_{\mathrm{deep}} = 1$, and (not shown) less than 1% for $J_{\mathrm{deep}} = 5$. Although a comparison between the experiments and numerical simulations can only be speculative, it is nonetheless interesting to note that when strong IGW excitation occurs the relative loss of momentum from the mixing region (7% in Experiment B) is comparable to estimates calculated in numerical simulations for moderate J_{deep}.

The numerical simulations clearly show that momentum is extracted from the mixing region most efficiently for a narrow range of values of J_{deep}. If the deep fluid is too weakly stratified, radiating IGW are not supported; if the deep fluid is too strongly stratified, IGW are generated but do not pump energy vertically away from the region on a sufficiently fast time scale. The radiation of IGW, and their effect back upon the mean flow, occurs most strongly when they propagate away from the mixing region at frequencies close the buoyancy frequency of the deep fluid.

6. Discussion and conclusions

The laboratory and numerical experiments demonstrate that significant momentum can be extracted from the mean flow in the mixing region if it is weakly stratified and the deep fluid is sufficiently strongly stratified. In an experiment in which large-amplitude IGW emission occurs, the flux of momentum from the mixing region is sufficiently large that we estimate the mean flow over the extent of the wavepacket decelerates by approximately 7% of the average flow across the shear depth during the emission time. The numerical simulations give values of the same order.

A result of the effect of wave excitation back upon the mean flow is that the largest amplitude waves are observed with their phase tilting at angles between 45° and 60° from the vertical. The preponderance of waves with angles about this range is explained here using linear theory.

For plane IGW, it is well known that the vertical group velocity is a maximum for waves propagating at 45° (e.g. Gill 1982, §6.8). Therefore, if the energy in the mixing region is evenly distributed across a wide frequency range, we expect that IGW excited at a frequency $\omega \simeq N_{\mathrm{deep}}/\sqrt{2}$ are capable of transporting the largest proportion of energy vertically away from the region. Suppose now that the waves are of sufficiently large amplitude that the mean flow is decelerated due to transport of momentum away from the mixing region by IGW. Thus as IGW continue to radiate, their excitation frequency decreases and their phase tilts more horizontally. If the forcing of IGW from the mixing region continues to occur at the same amplitude, energy is removed from the mixing region less rapidly and the feedback is reduced. Likewise the feedback is less effective if the IGW are forced at a frequency faster than $N_{\mathrm{deep}}/\sqrt{2}$. The key to understanding the preponderance of IGW with phase tilts in an a narrow frequency band appears to be coupling between radiating IGW and the mixing region which is most pronounced for $\omega \simeq N_{\mathrm{deep}}/\sqrt{2}$. Although a broad frequency spectrum of IGW may be excited, the waves close to this frequency extract energy from the mean flow most efficiently and therefore dominate the observed spectrum. More than this, it seems that these waves are capable of modifying the mean flow so that they continue to be excited, and waves of frequencies outside this band are suppressed. The detailed nature of the coupling between radiating IGW and the mean flow has yet to be explored in an analytic theory.

The authors would like to thank Stuart Dalziel for his assistance with the experimental set-up. We are grateful to one of the reviewers, whose comments helped us more clearly present a number of points in the original manuscript. This work has been supported by NERC under grant number GR3/09399.

REFERENCES

Alexander, M. J. 1996 A simulated spectrum of convectively generated gravity waves: Propagation from the tropopause to the mesopause and effects on the middle atmosphere. *J. Geophys. Res.* **101**, 1571–1588.

Bonneton, P., Chomaz, J. M. & Hopfinger, E. J. 1993 Internal waves produced by the turbulent wake of a sphere moving horizontally in a stratified fluid. *J. Fluid Mech.* **254**, 1–21.

Boyer, D. L., Davies, P. A., Fernando, H. J. S. & Zhang, X. 1989 Linearly stratified flow past a horizontal circular cylinder. *Phil. Trans. R. Soc. Lond.* A **328**, 501–528.

Brandt, P. B., Alpers, W. & Backhaus, J. O. 1996 Study of the generation and propagation of internal waves in the Strait of Gibraltar using a numerical model and synthetic aperture radar images of the European ERS 1 satellite. *J. Geophys. Res.* **101**(C6), 14237–14252.

Bretherton, F. P. 1969 Momentum transport by gravity waves. *Q. J. R. Met. Soc.* **95**, 213–243.

Castro, I. P., Snyder, W. H. & Baines, P. G. 1990 Obstacle drag in stratified flow. *Proc. R. Soc. Lond.* A **429**, 119–140.

Chimonas, G. & Grant, J. R. 1984 Shear excitation of gravity waves. Part I: Modes of a two-scale atmosphere. *J. Atmos. Sci.* **41**, 2269–2277.

Dalziel, S. B., Hughes, G. O. & Sutherland, B. R. 1998 Whole field density measurements. *Exps. Fluids* (in preparation).

Davis, P. A. & Peltier, W. R. 1979 Some characteristics of the Kelvin-Helmholtz and resonant overreflection modes of shear flow instability and of their interaction through vortex pairing. *J. Atmos. Sci.* **36**, 2394–2412.

Davis, R. E. 1969 The two-dimensional flow of a stratified fluid over an obstacle. *J. Fluid Mech.* **36**, 127–143.

Fovell, R., Durran, D. & Holton, J. R. 1992 Numerical simulations of convectively generated stratospheric gravity waves. *J. Atmos. Sci.* **49**, 1427–1442.

Fritts, D. C. 1982 Shear excitation of atmospheric gravity waves. *J. Atmos. Sci.* **39**, 1936–1952.

Gill, A. E. 1982 *Atmosphere-Ocean Dynamics*. Academic. 662 pp.

Huppert, H. E. & Miles, J. W. 1969 Lee waves in a stratified flow. Part 3. Semi-elliptical obstacle. *J. Fluid Mech.* **35**, 481–496.

Lacombe, H. & Richez, C. 1989 The regime of the Strait of Gibraltar. In *Hydrodynamics of Semi-Enclosed Seas* (ed. J. C. J. Nihoul), pp. 13–73. Elsevier.

Lilly, D. K. & Kennedy, P. J. 1973 Observations of a stationary mountain wave and its associated momentum flux and energy dissipation. *J. Atmos. Sci.* **30**, 1135–1152.

Lin, J. T. & Pao, Y. H. 1979 Wakes in stratified fluids. *Ann. Rev. Fluid Mech.* **11**, 317–338.

Lin, Qiang, Boyer, D. L. & Fernando, H. J. S. 1992 Turbulent wakes of linearly stratified flow past a sphere. *Phys. Fluids* A **4**, 1687–1696.

Linden, P. F. 1975 The deepening of a mixed layer in a stratified fluid. *J. Fluid Mech.* **71**, 385–405.

Lindzen, R. S. 1974 Stability of a Helmholtz velocity profile in a continuously stratified infinite Boussinesq fluid – applications to clear air turbulence. *J. Atmos. Sci.* **31**, 1507–1514.

Long, R. R. 1955 Some aspects of the flow of stratified fluids. III Continuous density gradients. *Tellus* **7**, 341–517.

McFarlane, N. A. 1987 The effect of orographically excited gravity wave drag on the general circulation of the lower stratosphere and troposphere. *J. Atmos. Sci.* **44**, 1775–1800.

Miles, J. W. 1968 Lee waves in a stratified flow. Part 1. Thin barrier. *J. Fluid Mech.* **32**, 549–567.

Odell, G. M. & Kovasznay, L. S. G. 1971 A new type of water channel with density stratification. *J. Fluid Mech.* **50**, 535–543.

Palmer, T. N., Shutts, G. J. & Swinbank, R. 1986 Alleviation of a systematic westerly bias in general circulation and numerical weather prediction models through an orographic gravity drag parametrization. *Q. J. R. Met. Soc.* **112**, 1001–1039.

Press, W. H., Flannery, B. P., Teukolsky, S. A. & Vetterling, W. T. 1993 *Numerical Recipes: The Art of Scientific Computing*, 2nd Edn. Cambridge University Press. 702 pp.

Smyth, W. D. & Peltier, W. R. 1989 The transition between Kelvin-Helmholtz and Holmboe instability: An investigation of the overreflection hypothesis. *J. Atmos. Sci.* **46**, 3698–3720.

Stevenson, T. N. & Thomas, N. H. 1969 Two-dimensional internal waves generated by a travelling oscillating cylinder. *J. Fluid Mech.* **36**, 505–511.

Sutherland, B. R. 1996 The dynamic excitation of internal gravity waves in the equatorial oceans. *J. Phys. Oceanogr.* **26**, 3214–3235.

Sutherland, B. R., Caulfield, C. P. & Peltier, W. R. 1994 Internal wave generation and hydrodynamic instability. *J. Atmos. Sci.* **51**, 3261–3280.

Sutherland, B. R., Dalziel, S. B., Hughes, G. O. & Linden, P. F. 1998 Visualization and measurement of internal waves by 'synthetic schlieren'. Part 1. Vertically oscillating cylinder. *J. Fluid Mech.* (submitted).

Sutherland, B. R. & Peltier, W. R. 1995 Internal gravity wave emission into the middle atmosphere from a model tropospheric jet. *J. Atmos. Sci.* **52**, 3214–3235.

Thorpe, S. M. 1966 Internal gravity waves. PhD thesis, University of Cambridge.